nature communications

Article

https://doi.org/10.1038/s41467-025-57890-8

Biosilicification-mimicking chiral nanostructures for targeted treatment of inflammatory bowel disease

Received: 13 October 2024

Accepted: 4 March 2025

Published online: 15 March 2025

Check for updates

Miao Xu[1,3], Wei Xin[2,3], Jiabin Xu[1], Anya Wang[1], Shuai Ma[1], Di Dai[2], Yidan Wang[1], Dongmei Yang[1], Lin Zhao[1] ✉ & Heran Li[1] ✉

The cascade reaction of lipopolysaccharides (LPS), cell-free DNA (cfDNA), and reactive oxygen species (ROS), drives the development of inflammatory bowel disease (IBD). Herein, we construct polyethylenimide (PEI)-L/D-tartaric acid (L/D-TA) complexes templated mesoporous organosilica nanoparticles (MON) (PEI-L/D-TA@MON) by mimicking biosilicification under ambient conditions within seconds. The chiral nanomedicines include four functional moieties, wherein PEI electrostatically attracts cfDNA, tetrathulfide bonds reductively react with ROS, silanol groups adsorb LPS, and L/D-TA enables chiral recognition and inflammatory localization. Following oral administration, PEI-L-TA@MON exhibiting preferential conformation stereoscopically matches with mucosa and anchors onto inflammatory intestine for lesion targeting. PEI-L-TA@MON eliminates LPS, ROS, and cfDNA, alleviating oxidative stress, inhibiting inflammatory cascade, and maintaining immune homeostasis to achieve IBD therapy. In addition, the rapid synthesis, low cost, energy-free preparation, negligible toxicity, satisfactory therapeutic effect, and facile conversion on therapeutic modes of PEI-L-TA@MON will bring changes for IBD treatment, providing research values and translational clinical prospects.

Inflammatory bowel disease (IBD), including ulcerative colitis (UC) and Crohn's disease (CD), is a chronic, persistent, and inflammatory gastrointestinal disorder[1,2]. The main clinical features include protracted diarrhea, abdominal pain, mucopurulent blood stool, weight loss, and systemic manifestations, that seriously affect the health and life quality of patients, increase the risk of colorectal cancer for 5–8 folds, and impose a severe worldwide public health burden[3,4].

In healthy colon mucosa, the epithelium layer, mucosal immune system, and gut microbiota are in dynamic equilibriums to maintain intestinal homeostasis. For the IBD-susceptible population, under complex interactions between genetic, environmental, and immune factors, the intestinal permeability increases, and intestinal antigens, bacteria, and other pathogens invade the mucous lamina propria, triggering an overly strong immune response, wherein abnormal activation of Toll-like receptors (TLRs) on effector immune cells drives the overproduction of inflammatory mediators that promote IBD[5–8]. Specifically, lipopolysaccharides (LPS) secreted by pathogenic bacteria is an important pathogen-associated molecular pattern (PAMP) activating immune cells for an inflammatory response via pattern recognition receptors such as Toll-like receptor-4 (TLR4) through the TLR4–myeloid differential protein-88 (MyD88)–nuclear factor B (NF-κB) signal pathway[4]. The aerobic respiration of immune cells in the intestinal mucosa of IBD patients produces large amounts of reactive oxygen species (ROS), which have been reported 10–100-folds higher concentrations than those in healthy individuals[9]. ROS then act as signal molecules to promote the infiltration of immune cells and the release of inflammatory factors, which not only directly causes tissue oxidative damage, disturbing the intestinal integrity, but also reacts with proteins and nucleotides, destroys the DNA structure, and induces apoptosis of cells[10]. The broken intestinal barrier enables the

[1]School of Pharmacy, China Medical University, Shenyang, China. [2]The First Hospital of China Medical University, Shenyang, China. [3]These authors contributed equally: Miao Xu, Wei Xin. ✉e-mail: zl_cmu@163.com; liheranmm@163.com

release of cell-free DNA (cfDNA) by damaged cells from organism and/or from gut bacteria in the intestine and the circulation of patients, which is recognized as a prognostic biomarker of IBD in clinic[11]. cfDNA is also a common damage-associated molecular pattern (DAMP) in the pathogenesis of IBD that activates immune cells through Toll-like receptor-9 (TLR9), causing the production of inflammatory factors and mediators, disturbing tissue homeostasis in the intestinal mucosa, and promoting the progression of colitis[12]. Therefore, LPS, ROS, and cfDNA, driven by genetic, immunological, and microbial issues, are the main upstream pathogenic factors of IBD that mediate the production of inflammatory factors, trigger proinflammatory signaling cascades, and inflict damage onto the intestine through multiple pathways. Even worse, these danger signals are close intertwined, mutual connected, and reciprocal causational, forming complex vicious cycles of IBD and leading to recurrent attacks and long-term illness[4,7]. Based on the pathogenesis of IBD, accumulating evidences have suggested that targeted scavenging the main upstream pathogenic factors can modulate the imbalanced immune response and represent a promising approach for the treatment of IBD.

Clinically, anti-inflammatory, immunomodulatory, and antidiarrheal drugs, including salicylic acids, glucocorticoids, immunosuppressive agents, biological agents, antibiotics, and montmorillonite powders, are often used for etiological and symptomatic treatments of IBD[12,13]. The above standard therapies are mainly aimed at regulating single factors or specific symptoms in the occurrence and development of IBD and fail to manage the vicious cycle of the disease caused by the main upstream pathogenic factors, thus exhibiting low remission rates and systemic side effects[14,15]. Besides, the application of immunosuppressive agents suppresses the normal immune response, reduces resistance to pathogens such as bacteria in the gut, and increases the risks of serious complications, including liver and kidney function impairments and opportunistic infections[16]. Regarding the drug-structural properties, the efficacies of either biological or small-molecular agents can be significantly affected by their stability, solubility, and permeability. Biological agents, such as tumor necrosis factor (TNF) antibodies and Janus kinase inhibitors, suffer from low stability, short half-life, and poor pharmacokinetic/pharmacodynamic properties, and must be frequently administered intravenously, resulting in poor patient compliance and undesirable clinical outcomes[17]. Conversely, the oral administration of therapeutic agents for the treatment of IBD has many clinically preferred merits, such as noninversion, convenience, safety, and more importantly, direct action on the target sites. Additional challenges are associated with the complex structure and physiological/pathological microenvironments of the gastrointestinal tract (GIT), which requires local drug release to ensure prolonged efficacy[18,19].

In recent years, nanomedicines with a broad spectrum of components, morphologies, and physicochemical traits have shown considerable potential in treating IBD. A number of studies have highlighted the preparation of drug-delivery systems by encapsulating therapeutic agents in nanoparticles (NPs) such as liposomes and solid lipid NPs to improve stability and solubility of drugs[20,21]. Furthermore, nanomedicines can be endowed with intelligent modes, such as stimuli-responsiveness and targeting ability based on the inflammatory microenvironments and/or colonic physiological characteristics, and multi-functionality through combining them with imaging particles (e.g., quantum dots and magnetic NPs) to improve their therapeutic and diagnostic potentials[21–23]. With the assistance of the biological or microbial matrixes (e.g., cells, biomembrane, exosomes, metabolites, and genetic components), nanoenzymes, as well as naturally plant-derived ingredients (e.g., epigallocatechin gallate, resveratrol, and berberine), more attractive IBD nanomedicines have been developed owing to their multiple biological functions including anti-inflammatory and microbiota regulatory abilities[24–27]. However, these complex drug-delivery systems or bioactive nanomedicines exhibit potential off-target effects, toxicities, and immunogenicities and encounter obstacles in assembly stability, quality control, and large-scale manufacturing.

Faced with an urgent need for more effective oral therapies of IBD, we hypothesize that nanomedicines involve scavenging of multiple pathogenic factors and maintaining a high concentration at the local inflammatory lesions in the GIT will bring substantial changes for IBD treatment[19]. Herein, we describe the in situ–controlled formation of chiral biosilica structures by manipulating a one-step biomimetic silica deposition (Fig. 1). Through a very simple mixing process of adding the inorganic/organic silica source to the chiral catalytic template polyethylenimide-L/D-tartaric acid (PEI-L/D-TA) solution, PEI-L/D-TA@MON is formed under neutral pH and ambient conditions within seconds. The reactants display multi-functionality corresponding to both mesoporous formation and disease treatment. As a proof-of-concept, we first investigate the structure, physicochemical and surface/interface properties of PEI-L/D-TA@MON, as well as theoretically and experimentally verify their capacities in scavenges various pathogenic factors in vitro. Then, the targeting and retention capacities of PEI-L/D-TA@MON, including the mucus permeation, bioadhesion, lesion penetration, and GIT retention are systematically evaluated in healthy mice, dextran sulfate sodium (DSS)-model mice and human ex vivo intestine from the perspective of lesion localization. Most importantly, the therapeutic effects and mechanisms of PEI-L/D-TA@MON against IBD in both prophylactic and delayed treatments are investigated in DSS-model mice. Particularly, PEI-L/D-TA@MON exhibiting mesoporous structures also provide abundant drug-loading sites in a sustained release manner, which can serve as a drug carrier to enable synergy therapy. Undoubtfully, PEI-L/D-TA@MON inspires alternative thinking for developing IBD nanomedicine and provides a reference for the treatment of other inflammatory diseases as well as intestinal lesions.

Results

Clinical data and patient samples of IBD

To investigate the clinical signs and colon damages caused by IBD, we first scanned the imaging manifestations. Under endoscopy, diffuse erosion and ulcers in the colon were intuitively observed for UC patients, while segmental lesions and longitudinal ulcers in the GIT were noticed for CD patients, indicating substantial damages to the intestinal barrier (Fig. 2a). The enterography (CTE) characteristics of IBD included the thickening of the intestinal wall with decreased echo, narrowed intestinal lumen, and emergence of the intestinal mucosal lesions (Fig. 2a). Lymphocyte subpopulation on UC and CD patients confirmed a dysfunction of the immune function, with a decreased number and proportion of CD4+ (signed to helper T-lymphocytes) cells, a slightly rise in CD8+ (related to cytotoxic T-lymphocytes) cells, and a decrease in the TH/S ratio (Fig. 2b). Further studies on the expression of T cells (CD8/CD4/Tbet/GATA-3) and CD4+ T cells (CD4/Tbet/GATA-3/FoxP3) via multiplex immunofluorescent (IF) staining on the colon tissues of IBD patients showed increased CD4+ cells, with an exacerbated Th1 response in CD patients, and a rise Th2 response in UC patients (Supplementary Figs. 1, 2). Single-cell transcriptome sequencing indicated significant increases in inflammatory-associated macrophages in both number and transcriptional heterogeneity compared with those in healthy tissues. The macrophage population was further subdivided the macrophage population according to M1 (PTGS2, CCL3, CD40 and CD86) and M2 (CD163,C1QA and MRC1) macrophage makers, and found significantly raised M1 macrophages proportion from 21% to 69% in UC patients, and from 12% to 74% in CD patients compared to healthy persons (Supplementary Figs. 3, 4). Subsequently, we collected serum from normal persons and IBD patients (Supplementary Table 1) and quantitatively measured the cfDNA, LPS and H_2O_2 concentrations. According to Fig. 2c, both UC and CD patients showed 1.3 to 3.3-, 0.7 to 5.1-, and 1.4 to 3.5-folds higher

https://doi.org/10.1038/s41467-025-57890-8

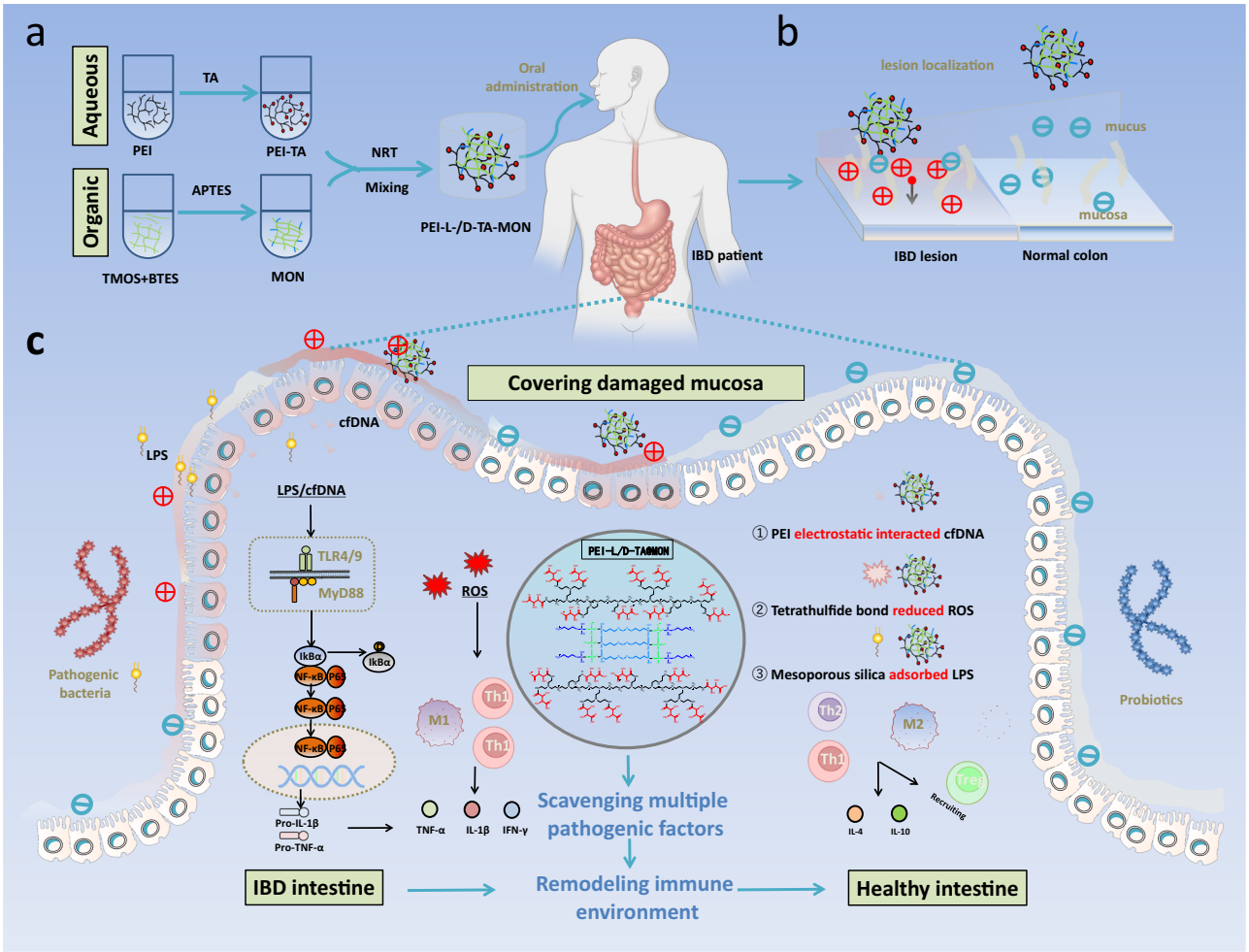

Fig. 1 | Schematic illustration on PEI-L/D-TA@MON for the treatment of IBD. **a** A biosilicification-mimicking route to form chiral nanostructures PEI-L/D-TA@MON. **b** The lesion localization strategy for targeted delivery of PEI-L/D-TA@MON. **c** Mechanisms on the generation (inflammatory cascade driven by the LPS, cfDNA and ROS) and prevention (scavenging pathogenic factors to suppress inflammation) of IBD. TA tartaric acid, TMOS tetramethyl orthosilicate, APTES 3-aminopropyltriethoxysilane, BTES bis[3-(triethoxysilyl)propyl] tetrasulfide, NPT normal pressure and temperature.

serum levels of cfDNA, LPS and H_2O_2 than those of healthy volunteers. Patients in active phase had higher serum pathogenic factor levels compared to patients in stationary phase (Fig. 2d). Furthermore, serum cfDNA, LPS and H_2O_2 levels were collectively positively correlated with C-reactive protein (CRP), as a common index to reflect inflammatory degree in clinic (Fig. 2e, Supplementary Fig. 5).

We then carried out hematoxylin and eosin (HE), immunohistochemistry (IHC) and IF staining on the intestinal samples from UC and CD patients to illustrate the pathological feature and inflammatory microenvironment of IBD (Supplementary Table 2). HE images showed a decrease or disappearance of intestinal mucosal recess, lesions on the mucosal basal or submucosal inflammatory, and an increase in plasma cell number in the intestinal mucosa for IBD patients (Fig. 2f). Compared to healthy intestines, IBD patients showed higher frequencies of lamina propria TLR4+, Toll-like receptor-5 (TLR5) + and TLR9+ cells and potential pathways of TLR4/TLR9–MyD88–NF-κB activated by LPS and cfDNA as shown in the IHC staining images (Fig. 2g and Supplementary Fig. 6). Dihydroethidium (DHE) and transferase dUTP nick end labeling (Tunel) staining showed pronounced red and green fluorescence signals, respectively, highlighting ROS production and cell apoptosis (Fig. 2h, i). Subsequent multiplex IF staining showed imbalanced intestinal homeostasis and inflammatory microenvironments, wherein significant activation of neutrophils and macrophages (mainly M1 macrophages) as well as impaired endothelial integrity were marked by increased levels of myeloperoxidase (MPO), CD68 and CD86, and decreased levels of CD31 (Fig. 2j, Supplementary Fig. 7). Thus, according to the reported pathogenesis and analyses on the clinical data and patient samples, we reasoned that LPS, ROS, and cfDNA are the main upstream pathogenic factors of IBD.

Biomimetic synthesis of PEI-L/D-TA@MON

Targeted scavenging LPS, ROS and cfDNA for IBD treatment, PEI-L/D-TA@MON exhibiting chiral biosilica structures were meticulous designed and controllable formed via a bottom-up biosilicification-mimicking strategy under neutral pH and ambient conditions. We first grafted L/D-tartaric acid (L/D-TA) onto PEI via nucleophilic substitution by directly adding L/D-TA into the PEI solution at room temperature, wherein the –COOH groups of TA and the –NH– sites of PEI dehydration condensed to form amido linkages (Fig. 3a). As verified by Fourier-transform infrared spectroscopy (FTIR) spectroscopy, absorption bands of ν-NH (3265.7 cm^{-1}) and δ-N–H (1635.1 cm^{-1}) were observed in the spectra of PEI, while bands of ν-NH disappeared and replaced by those of ν-OH (3403.8 cm^{-1}), ν-CONH (3157.4 cm^{-1}), ν-C = O (1726.2 cm^{-1}, belonging to the carboxyl group) and of ν-C = O (1600.6 cm^{-1}, assigned to amido-I) in the spectra of PEI-L/D-TA (Fig. 3e). In addition, after L/D-TA modification, decreases in the zeta potential of the PEI solution agglutination occurred from 18.0 to 13.5 and 10.7 mV, indicating the association of positively charged PEI with

https://doi.org/10.1038/s41467-025-57890-8

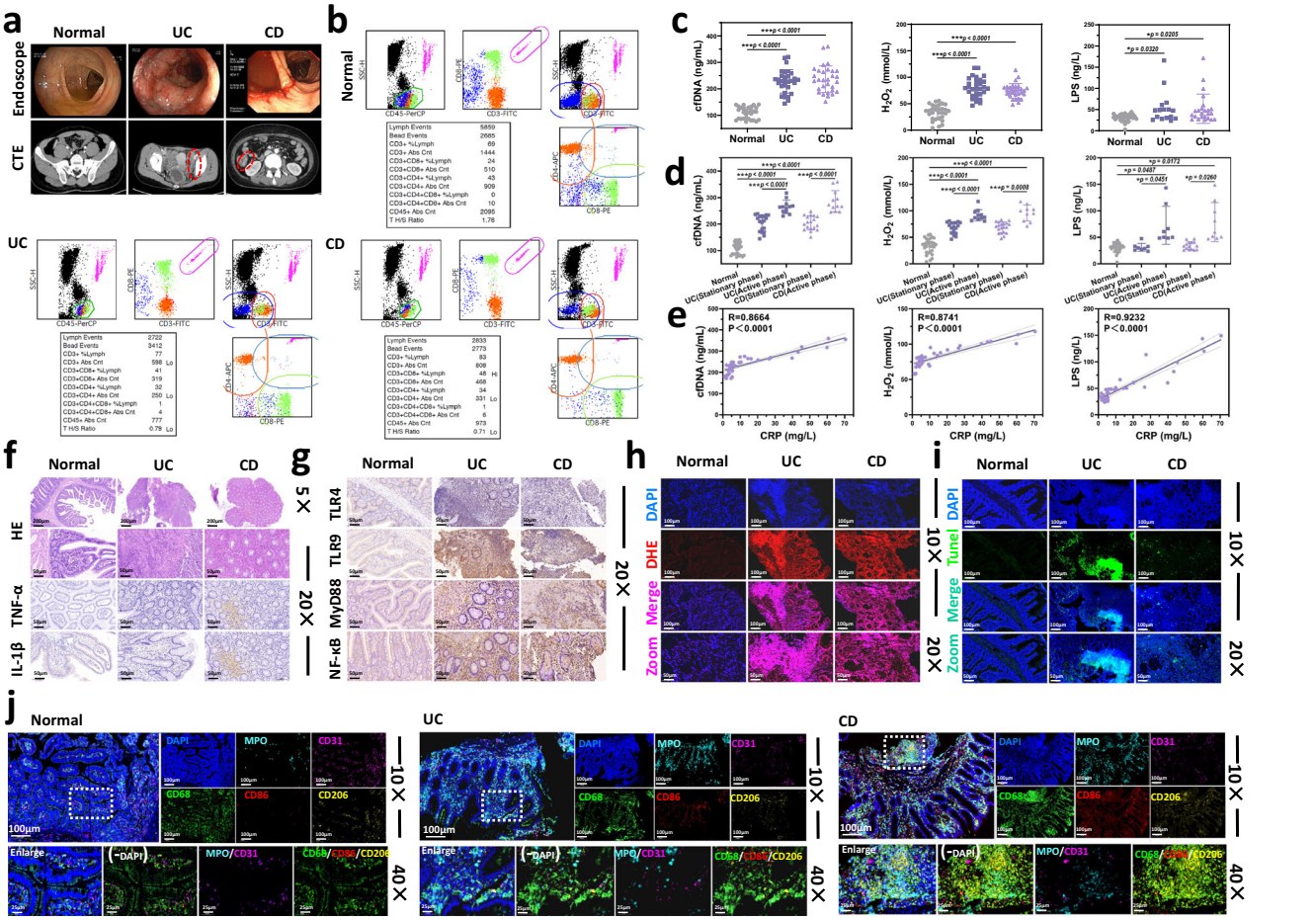

Fig. 2 | Clinical specimens confirmed the immune activation and pathogenic factors of IBD. a The endoscopy and CTE images of IBD (including UC and CD) patients, with red arrows indicating the focus in colon. **b** Lymphocyte subpopulation on IBD patients to confirm the immune state. **c** Serum levels of pathogenic factors (including cfDNA, H_2O_2 and LPS) in IBD patients ($n = 60$). **d** Serum levels of pathogenic factors in IBD patients in active or stationary phases ($n = 60$). **e** Linear regression curves to illustrate the correlation between serum cfDNA, H_2O_2 and LPS levels and CRP. **f** HE staining and (**g**). IHC staining (corresponding to TNF-α and IL-1β, TLR4, TLR9, MyD88, NF-κB expressions) of colon tissues from IBD patients ($n = 12$). **h** DHE and (**i**) Tunel staining of colon tissues from IBD patients ($n = 12$); blue: nucleus stained with 4,6-diamidino-2-phenylindole (DAPI), red: ROS, green: apoptotic cells. **j** Multiplex IF staining of colon tissues from IBD patients ($n = 6$); blue: nucleus stained with DAPI, light blue: neutrophil stained with MPO, pink: endotheliocyte marked with CD31, green: macrophages marked with CD68, red: M1 macrophages marked with CD86, and yellow: M2 macrophages marked with CD206. Data presented as the mean ± SD. $^*P < 0.05$ and $^{**}P < 0.01$ and $^{***}P < 0.001$ by two-tailed Student's *t* test. Source data are provided in the Source Data file.

negatively charged carboxyl groups (Supplementary Fig. 8). The alkoxysilane sites of the tetrasulfur-bridged organic silica source BTES polymerized with inorganic TMOS in ethanol. Through a very simple mixing process of adding the inorganic/organic silica source to the PEI-L/D-TA solution, PEI-L/D-TA@MON was rapidly formed within a few seconds at high yields (Fig. 3b). From a direct observation on the appearance of the products, a rapid gelation of PEI-L/D-TA@MON was noticed after the addition of BTES/TMOS. PEI-L/D-TA, which contains a large amount of basic amines and carboxyl groups on its surface, was efficient at simultaneously serving as a catalyst, scaffold, and template to promote the hydrolysis of alkoxysilane and silica deposition[28–30]. This unique approach satisfied the biomimetic requirement for both the production of silica under ambient conditions and the precise control over mesoporous formation within both temporal and spatial scales[31,32]. PEI-L/D-TA@SiO_2 with the absence of tetrathulfide bonds, and PEI@SiO_2 lacked both tetrathulfide bonds and chiral ligands, were also prepared for comparative study.

As vividly seen in the transmission electron microscopy (TEM) and scanning electron microscopy (SEM) images, all nanomedicines formed intensively aggregated NPs (10–20 nm, accounting for the maximum percentage) with the existence of abundant nanopores distributed around the surface (Fig. 3c). PEI-L/D-TA@MON presented characteristic absorption at 3355.9, 1102.9, 458.1, 1622.5, 1080.2, and 557.5 cm^{-1} in the FTIR spectra, ascribing to ν-Si–O–Si, ν-Si–OH, δ–Si–O–Si, ν-N–H, ν-C–S, and ν-S–S bonds, respectively (Fig. 3f). The functional moieties were effectively imprinted along with silica deposition, and X-ray photoelectron spectroscopy (XPS) spectra showed elemental peaks of Si, C, O, N, and S (Fig. 3g, Supplementary Fig. 9). Synergistically, energy dispersive spectroscopy (EDS) mapping images disclosed the uniform elemental distribution with contents of 15.6% (Si), 47.6% (C), 28.8% (O), 1.8% (N), and 6.3% (S) (Fig. 3d, i). As a matter of course, PEI-L/D-TA@MON displayed the most potent weight loss (54.8%) in the thermogravimetric analysis (TGA) curves compared to PEI@SiO_2 (14.0%) and PEI-L/D-TA@SiO_2 (18.6%), because of the crosslinking of the organic silica source (Fig. 3h). The mesoporous structure of PEI-L/D-TA@MON was studied by nitrogen adsorption/desorption tests, wherein distinct type IV adsorption/desorption isotherms with hysteresis loops were observed for PEI@SiO_2, PEI-L-TA@SiO_2 and PEI-D-TA@SiO_2 (Supplementary Fig. 8). Small-angle X-ray diffraction (SAXD) analysis indicated the mesoporous structure of these nanomedicines, while X-ray diffraction (XRD) study confirmed their amorphous nature (Supplementary Fig. 8). Compared to

https://doi.org/10.1038/s41467-025-57890-8

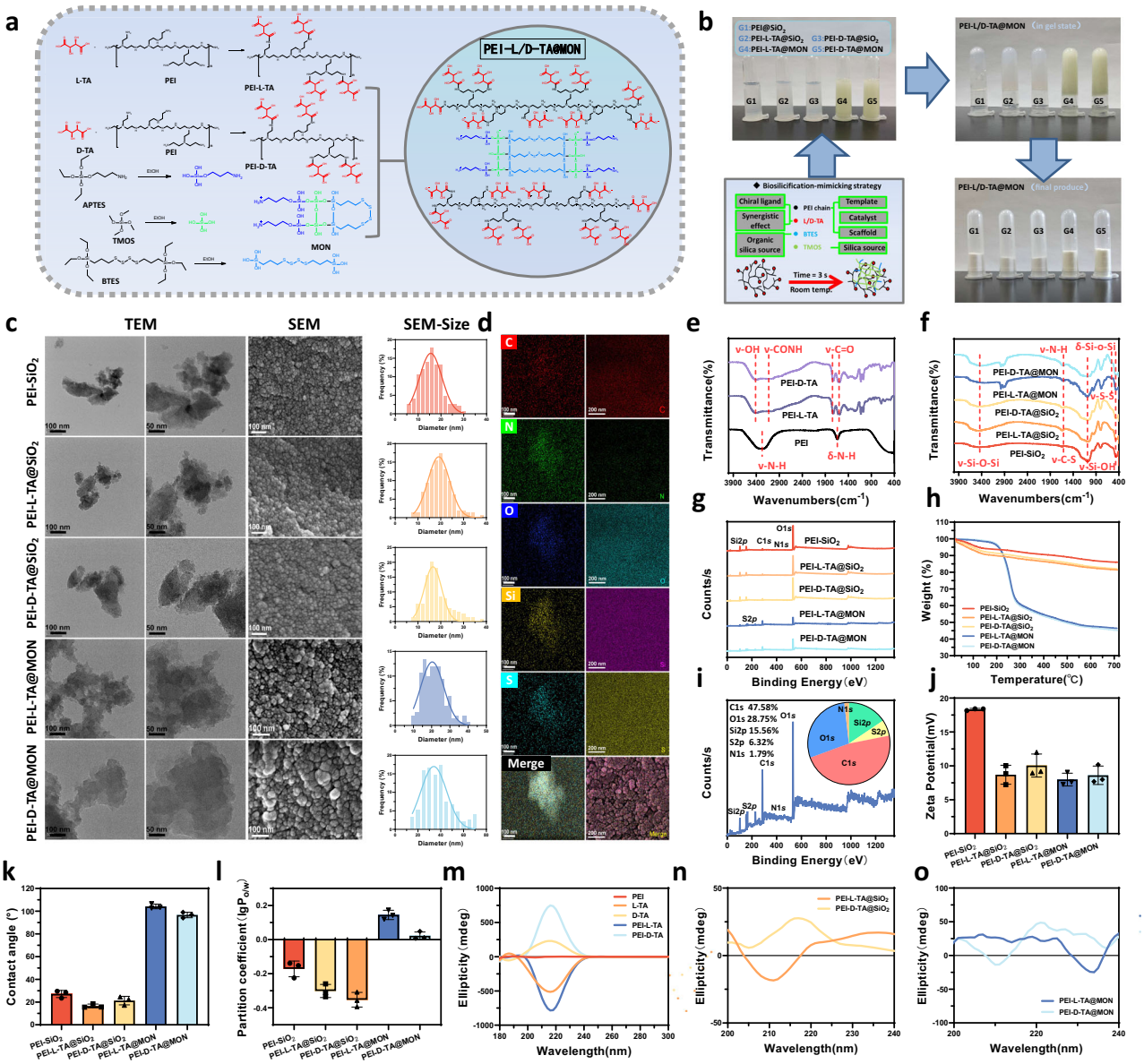

Fig. 3 | Biomimetic synthesis and characterization of PEI-L/D-TA@MON. **a** Molecular mechanism for the synthesis of PEI-L/D-TA@MON. **b** Appearances of the PEI-L/D-TA@MON in different stages. **c** TEM, SEM images, and the particle size distribution (each counted from 200 NPs in the SEM images) of the nanomedicines. **d** EDS mapping images of PEI-L-TA@MON. **e** FTIR spectra of PEI-L/D-TA. **f** FTIR spectra. **g** XPS spectra and (**h**). TGA curves of PEI-L/D-TA@MON. **i** EDS spectra and element distribution of PEI-L-TA@MON. **j** Zeta potential, **k** Initial contact angle and (**l**). oil-water partition coefficients of PEI-L/D-TA@MON. Circular dichroism (CD) spectra of **m**. PEI-L/D-TA, **n** PEI-L/D-TA-SiO_2 and (**o**) PEI-L/D-TA-MON. Experiments were repeated three times independently with similar results. Data presented as the mean ± SD. Source data are provided in the Source Data file.

PEI@SiO_2, the L/D-TA modification decreased the zeta potential, and the BTES crosslink increased the surface hydrophobicity as evidenced by the enhanced oil–water partition coefficients and contact angles (Fig. 3j–l, Supplementary Fig. 10, 11). More importantly, the chirality of L/D-TA exhibited a negative and positive Cotton effect, which derived to PEI-L/D-TA and ultimately imprinted along with silica deposition by employing PEI-L/D-TA as the scaffold, template, and catalyst (Fig. 3m–o).

PEI-L/D-TA@MON scavenges various pathogenic factors in vitro

To illustrate the surface/interface interactions and potential chiral recognition between PEI-L/D-TA@MON and the pathogenic factors, we conducted molecular dynamics (MD) simulations. Firstly, organic/inorganic silica source model and PEI-L/D-TA model combined by L/D-TA molecule and PEI chain were formed (Supplementary Fig. 12). Afterwards, PEI-L/D-TA was used to build a scaffold, and the silica source model was allowed to deposit onto the scaffold to obtain the PEI-L/D-TA@MON sheet (Fig. 4a). The structures of LPS, cfDNA, H_2O_2, and endogenous chiral substances were simplified to lipid A (as the bioactive center and main toxic component of LPS), nucleotide (as the basic unit of DNA), H_2O_2, and L/D-alanine (L/D-Ala), respectively, and their electrostatic potentials were analyzed (Fig. 4a, Supplementary Fig. 13). Then, the pathogenic factors were adsorbed onto PEI-L/D-TA@MON via MD simulation, wherein the negative binding energy (E_{INT}) demonstrated significant adsorption effects (Fig. 4b, c, Supplementary Figs. 14–17, Supplementary Table 6). PEI-L-TA@MON, as the preferential conformation, showed stronger E_{INT} on lipid A, nucleotide, H_2O_2, L-Ala, and D-Ala (−1792.5, −2054.8, −2236.7, −2045.0, and −1913.7 kcal/mol, respectively) than those of PEI-D-TA@MON (−1773.0, −2043.5, −2038.4, −1812.9, and −1841.6 kcal/mol, respectively), which

https://doi.org/10.1038/s41467-025-57890-8

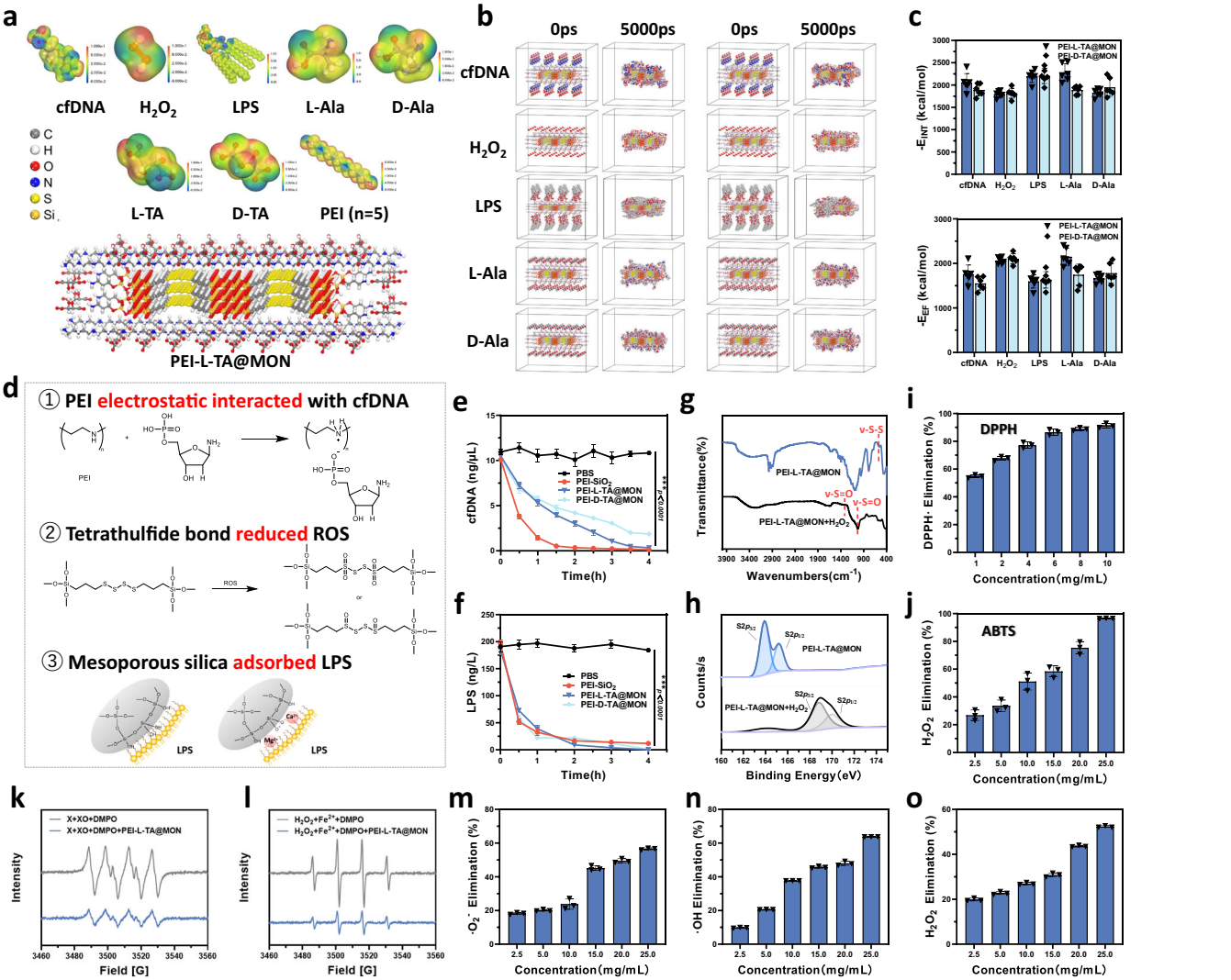

Fig. 4 | Pathogenic factors scavenging properties of PEI-L/D-TA@MON. **a** Molecular model and electrostatic potential of the pathogenic factors and PEI-L/D-TA@MON. **b** MD simulation on the adsorbing of pathogenic factors onto PEI-L/D-TA@MON. **c**The E_{INT} and electrostatic force (E_{EF}) of the adsorbing of pathogenic factors onto PEI-L/D-TA@MON. **d** Equations on the scavenging of various pathogenic factors. Time-dependent (**e**). cfDNA and (**f**) LPS scavenging capacities of nanomedicines. Data are presented as the mean ± SD ($n = 3$ independent experiments). ***$P < 0.001$ by two-tailed Student's t test. **g** FTIR and **h**. XPS spectra of PEI-L-TA@MON before and after incubation with H_2O_2. Concentration-dependent antioxidant ability of PEI-L-TA@MON measured using (**i**) ABTS and (**j**) DPPH. **k** EPR spectra of the mixed solution of xanthine (X), xanthine oxidase (XO), and 5,5-dimethyl-1-pyrroline-N-oxide (DMPO) in the absence and presence of PEI-L-TA@MON. **l** EPR spectra of the mixed solution of Fe^{2+}, H_2O_2, and 5,5-dimethyl-1-pyrroline-N-oxide (DMPO) in the absence and presence of PEI-L-TA@MON. Concentration-dependent ROS radicals (**m** H_2O_2, **n** ·OH, and **o** $\cdot O_2^-$) scavenging capacities of PEI-L-TA@MON. Experiments were repeated three times independently with similar results. Data presented as the mean ± SD. $n = 3$, ***$p < 0.001$. Source data are provided in the Source Data file.

was attributed to the different steric hindrance on their surface/interface (Fig. 4c). Furthermore, electrostatic forces dominated most of the adsorptions. Van der Waals force contributed the largest percentage (~28%) in the LPS adsorption because of the multiple carbon chains with weak polarity in the molecular structure of LPS (Supplementary Fig. 18, Supplementary Table 7). In addition, a large number of hydrogen bonds were formed between PEI-L/D-TA@MON and the pathogenic factors (Supplementary Table 9).

The adsorption ability of PEI-L-TA@MON was first verified by the fading of dye colors after incubating with rhodamine B (RhB) and evans blue (EB) (Supplementary Fig. 19). We explored the chiral recognition of PEI-L/D-TA@MON via the adsorption of L/D-Ala enantiomers. Compared with PEI-D-TA@MON, PEI-L-TA@MON showed a significantly increased adsorption of L-Ala (Supplementary Fig. 20). We then experimentally investigated the capacity of PEI-L/D-TA@MON in scavenging the pathogenic factors in vitro. PEI with secondary amine electron pairs had electron-donating appetency and was easily ionized to present a positive charge (Fig. 4d). It would electrostatically interact with the negatively charged phosphate groups on DNA or RNA, thus routinely serving as nonviral gene carriers[33–35]. Employing PEI@SiO_2 and PEI-L-TA@MON as scavengers, calf thymus DNA (ctDNA, used as a model DNA) was almost completely removed within 4 h, wherein the clearance rate of PEI-L-TA@MON was slightly higher than that of PEI-D-TA@MON in accordance with the MD simulation (Fig. 4e). Furthermore, all nanomedicines could effectively scavenge LPS (Fig. 4f).

PEI-L/D-TA@MON effectively scavenged ROS in the oxidation environment because the tetrasulfur bonds were oxidized to sulfoxide or sulfone with good hydrophilicity, thus showing a higher degradation rate (Supplementary Figs. 21–23)[36,37]. After incubating PEI-L/D-TA@MON in an oxidation environment (a H_2O_2-containing medium), absorption band of the tetrasulfur bond around 557.0 cm^{-1} disappeared, and bands assigned to sulfoxide (v-S = O, 1027.3 cm^{-1}) and

https://doi.org/10.1038/s41467-025-57890-8

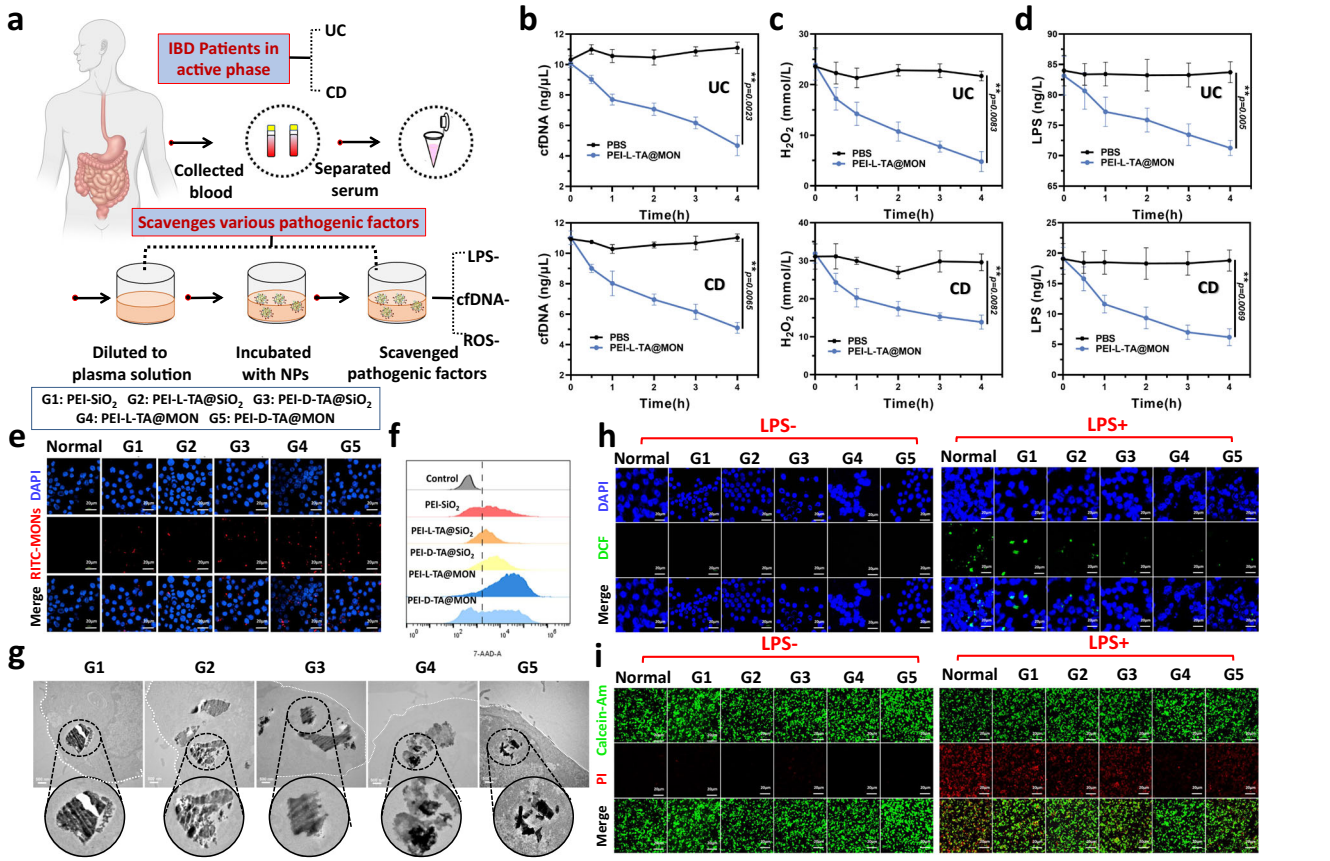

Fig. 5 | Pathogenic factors scavenging properties and intracellular antioxidant effect of PEI-L/D-TA@MON. a Schematic illustration on the scavenging of pathogenic factors by PEI-L-TA@MON in the serum of IBD patients. Time-dependent (**b**), cfDNA, (**c**) H_2O_2 and (**d**) LPS scavenging capacities of PEI-L-TA@MON in the serum of IBD patients. Data are presented as the mean ± SD ($n = 3$ independent experiments). $^{**}P < 0.01$ by two-tailed Student's t test. **e** CLSM images and (**f**) FCM analysis, and (**g**) bio-TEM images on the cellular uptake of PEI-L/D-TA@MON on RAW 264.7 cells; blue: nuclei stained with DAPI, red: rhodamine isothiocyanate (RITC) labeled nanomedicines. **h**DCF (blue: nuclei stained with DAPI, green: intracellular ROS) and (**i**) Calcein-AM/PI (blue: nuclei stained with DAPI, green: live cells, red: dead cells) staining images of LPS free (LPS-) or LPS treated (LPS +) RAW 264.7 cells with nanomedicines therapy. The data are presented as means ± SD, $n = 3$, $^{**}p < 0.01$. Source data are provided in the Source Data file.

sulfone (v-S = O, 1350.1 cm^{-1}) emerged in the FTIR spectra, while the sulfur valence changed from 2 to 4–6 in the XPS pattern (Fig. 4g, h). Oxidation of TMB by H_2O_2 produced oxidized 3,3′,5,5′-tetramethylbenzidine (TMB), which exhibited a characteristic absorption peak at 652 nm and simultaneously changes from colorless to blue, a reaction that can be facilitated by the catalytic effect of PEI-L/D-TA@MON on H_2O_2 (Supplementary Fig. 24)[34,38]. We also evaluated the antioxidant ability of PEI-L/D-TA@MON via azino-bis(3-ethylbenzothiazoline-6-sulfonic acid (ABTS) and 2,2-diphenyl-1-picrylhydrazyl (DPPH) tests, and noticed apparent color changes from blue to colorless, and from violet to light yellow for ABTS and DPPH tests, respectively (Fig. 4i, j, Supplementary Figs. 25, 26). Moreover, electron paramagnetic resonance (EPR) spectroscopy was used to qualitatively evaluate the single radical scavenging[35,39], and the results further demonstrated the effective ·OH, and·O_2^- scavenging capacity of PEI-L-TA@MON (Fig. 4k, l). Quantitatively, we then studied the capacity of PEI-L/D-TA@MON in eliminating single free radical reduced (including H_2O_2, ·OH, and ·O_2^-). The results discovered that, PEI-L-TA@MON reduced the levels of various radicals in a concentration-dependent manner (Fig. 4m–o).

As a proof of concept, we collected serum from IBD patients and used PEI-L-TA@MON to eliminate various pathogenic factors (Fig. 5a). As expected, PEI-L-TA@MON gradually decreased the levels of cfDNA, ROS, and LPS via electrostatic interaction, redox reaction, and adsorption, respectively, highlighting its potential to be a powerful nanomedicine for IBD treatment (Fig. 5b–d).

PEI-L/D-TA@MON ameliorates intracellular oxidative stress and inflammation

Taking into account the intestinal physiological and pathological microenvironments, RAW 264.7 cells (as macrophages are a critical cell type in directing host inflammatory and immune processes) and Caco-2 cells (as a widely accepted cell model with similar structure and biochemical characteristics to those of human intestinal epithelial cells) were involved in this study[40]. The cell counting kit-8 (CCK-8) assay showed high levels of cell viability (>85%) within the tested range of 5–80 μg/mL, demonstrating favorable cytocompatibility for both RAW 264.7 and Caco-2 cells (Supplementary Figs. 27, 28). 7′hdichlorofluorescein diacetate (DCF) staining and fluorescence live/dead assay suggested insignificant influences on cellular homeostasis after cell exposure to the nanomedicines (Fig. 5h, i). For in vitro and in vivo tracing, nanomedicines were labeled with RITC through stable covalent bonds (Supplementary Figs. 29, 30). The internalization efficiency of the nanomedicines was qualitatively and quantitatively investigated via confocal fluorescence microscopy (CLSM) and flow cytometry (FCM) after 4 h incubation. According to Fig. 5e and Supplementary Figs. 31, 32, a larger fraction of PEI-L-TA@MON (up to 78.3% and 75.9%) was uptake by RAW 264.7 and Caco-2 cells, and the intracellular fluorescence intensity was 2.1-, 1.6-, 1.6-, and 1.2-folds and 1.5-, 1.1-, 1.1-, and 1.2-folds higher than that of PEI@SiO_2, PEI-L-TA-@SiO_2, PEI-D-TA-@SiO_2, and PEI-D-TA@MON in RAW 264.7 and Caco-2 cells, respectively. The internalization efficiency was measured via FCM as 33.6%, 13.6%, 38.1%, 77.9%, and 53.2%, and 27.3%, 33.1%, 24.1%, 72.5%, and 52.3%

for PEI@SiO_2, PEI-L-TA-@SiO_2, PEI-D-TA-@SiO_2, PEI-L-TA@MON, and PEI-D-TA@MON in the two types of cells, respectively (Fig. 5f and Supplementary Figs. 31, 33). Although the multiple modifications of PEI-L-TA@MON reduced the zeta potential of the nanomedicine, it still showed marked uptake amounts, because the hydrophobic surface had a higher affinity with the cell membrane and the artificial chiral nanostructures produced enantioselective interactions[41–43]. As directly seen in the bio-TEM images, nanomedicines as aggregated NPs were effectively internalized by cells and distributed inside the cells without significant NPs degradation or destruction on the cellular structure (Fig. 5g). To study the host inflammatory and immune processes, LPS was applied to induce intracellular inflammation. A large amount of intracellular ROS was produced after LPS stimulation, as pointed out by the green fluorescence signal from DCF staining (Fig. 5h). However, the intracellular ROS level was significantly decreased with the therapy of PEI-L/D-TA@MON, highlighting the distinct ROS-elimination ability. Simultaneously, LPS disrupted the oxidative stress balance and caused massive cell death (Fig. 5i). PEI-L/D-TA@MON protected cells from the threat of LPS and resembled the intracellular redox homeostasis with almost no dead cells, which was further proved by the CCK-8 assay (Supplementary Fig. 34). We also used H_2O_2 to disrupt the cellular oxidative stress balance, and noticed the protective effect of PEI-L/D-TA@MON against H_2O_2 irritation (Supplementary Fig. 35). In addition, the level of proinflammatory cytokine tumor necrosis factor α (TNF-α) was downregulated, whereas the antioxidant enzymes superoxide dismutase (SOD, defended ROS with the ability to convert $\cdot O_2^-$ into H_2O_2 and O_2), and catalase (CAT, decomposed H_2O_2 into O_2 and H_2O) activities were enhanced (Supplementary Figs. 36, 37). Compared to PEI-D-TA@MON, PEI-L-TA@MON was more capable of ameliorating intracellular oxidative stress and inflammation, which was attributed to its higher cell internalization efficiency.

Mucus coverage and penetration of PEI-L/D-TA@MON

Inspired by the scavenging efficiency of the nanomedicines, we explored their GIT retention and lesion localization (Fig. 6a). Mucus with a viscoelastic tenacious mesh structure is known to cover the surface of intestinal mucosa, protect the intestinal homeostasis, and set physical limitations for the entrance of drugs and/or NPs into the

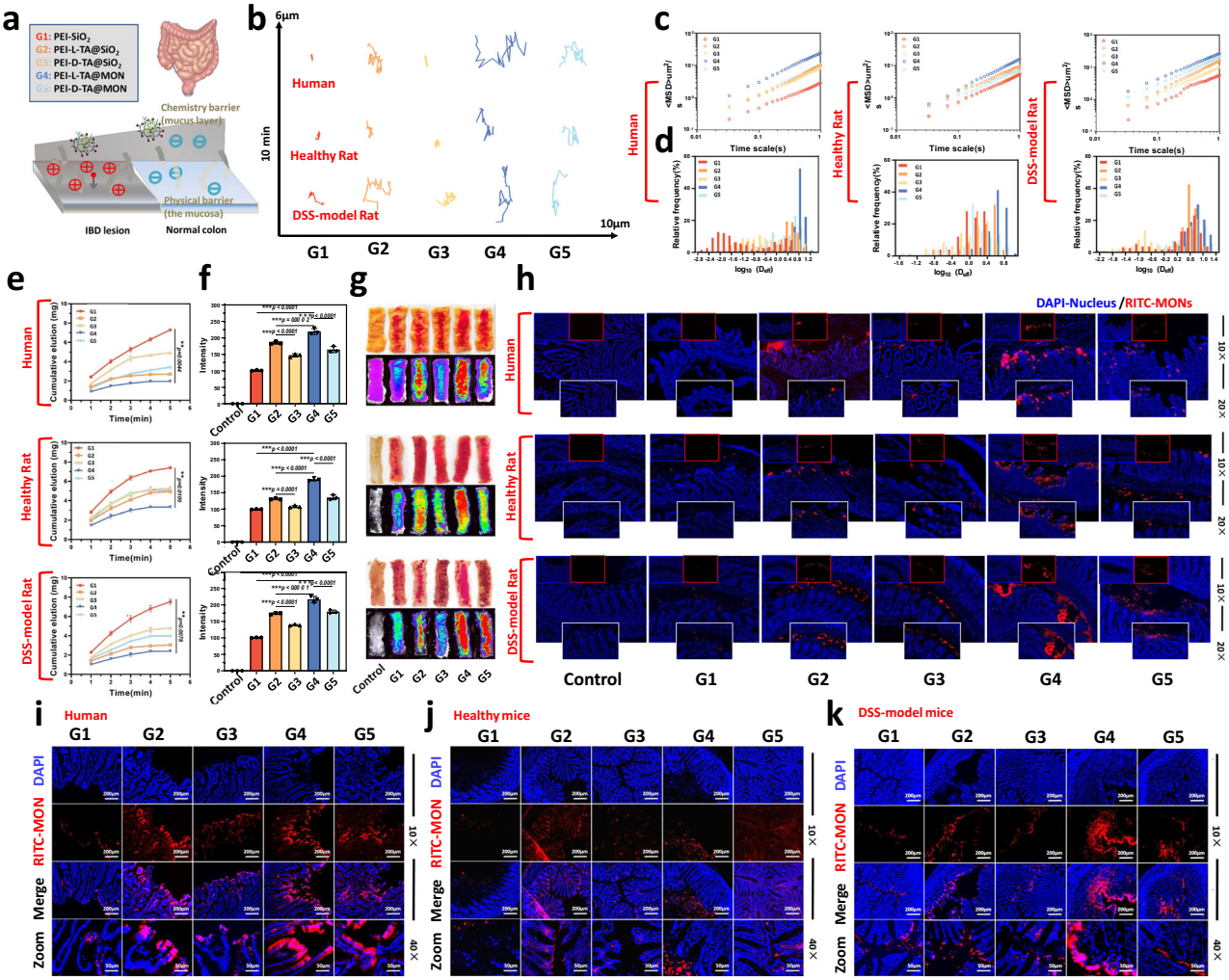

Fig. 6 | Mucus coverage and penetration of PEI-L/D-TA@MON. a Schematic illustration on the permeation of nanomedicines at the colon. **b** Representative trajectories, **c** MSD and (**d**) distributions on the logarithms of effective diffusivities (Deff) of nanomedicines penetrated in the mucus of human, healthy rat or DSS-model rat at a time scale of 10 min. At least 100 particles of each type were tracked per sample. **e** Elution time curve, (**f**) mucosal adhesion amount, data are presented as the mean ± SD ($n = 3$ independent experiments). ***$P < 0.001$ by two-tailed Student's t test, **g** appearance and fluorescence images, and (**h**) CLSM images of nanomedicines remained on the intestinal mucosa of human, healthy rat or DSS-model rat; blue: nuclei stained with DAPI, red: RITC labeled nanomedicines. CLSM images on the permeation of nanomedicines at the **i**. ex vivo intestine of human at 1.5 h post incubation, and at the colon of (**j**) healthy or (**k**) DSS-model mice at 2 h post-oral administration; blue: nuclei stained with DAPI, red: RITC labeled nanomedicines. $n = 3$ biologically independent animals. The data are presented as means ± SD, *$p < 0.05$, **$p < 0.01$, and ***$p < 0.001$. Source data are provided in the Source Data file.

intestinal mucosa[44–46]. We employed viscous glycerol (Gly), cross-linked hydroxyethyl cellulose (HEC), chiral L-Ala, oxidative H_2O_2, and rat- or human-sourced mucus to simulate the influence factors in both physiological and inflammatory mucus, as viscosity, space limitation, chirality, oxidation, and animal species, respectively. Nanomedicines were labeled with RITC and exposed onto the top layer of a 2-cm thick mediums, and allowed to freely diffuse for 24 h (Supplementary Fig. 38). In the human and rat mucus as well as under the simulated physiological conditions, PEI-L-TA@SiO_2 exhibiting neutral charged surface and preferential conformation showed the highest penetration efficiency (except in HEC medium, wherein particle size and shape were the decisive factors), while PEI@SiO_2 with a positive surface charge was restricted to the upper layers of the mediums. In the simulated pathological environment containing H_2O_2, PEI-L-TA@MON with ROS responsivity produced the best mucus penetration, which was 1.7-, 1.2-, 1.3-, and 1.2-folds higher than that of PEI@SiO_2, PEI-L-TA-@SiO_2, PEI-D-TA-@SiO_2 and PEI-D-TA@MON, respectively. We proceeded to analyze the particle trajectories, diffusion rates, and diffusion efficiencies via multiple particles tracking technology. According to Fig. 6b, PEI@SiO_2 with a positive charge was easily captured by the negatively charged mucus, thus showing restricted and irregular Brownian movement trajectories in short distances within 10 min. Conversely, PEI-L/D-TA-@SiO_2 and PEI-L/D-TA@MON moved freer and faster over longer distances. It is apparent that, PEI-L/D-TA@MON had the highest individual mean square displacement (MSD) with uniform distribution when incubated with rat or human mucus, which was 2.9- to 8.7-times higher than the competitors within 10 min, respectively (Fig. 6c, d).

Subsequently, RITC-labeled nanomedicines were allowed to permeate through the mucus layer (which was stained with fluorescein isothiocyanate [FITC]) in the fresh ex vivo rat or human intestinal tubes, and monitored by CLSM. Conforming to the in vitro mucus penetration trends, we found significantly stronger red fluorescence signals of PEI-L-TA@SiO_2 and PEI-L-TA@MON than the competitors from a direct observation in z-stack mode, suggesting the chiral recognition (Supplementary Fig. 39). Noticeably, in the intestinal tubes of IBD-model rats, the penetration depths of PEI@SiO_2, PEI-L-TA-@SiO_2, PEI-D-TA-@SiO_2, PEI-L-TA@MON, and PEI-D-TA@MON in the z-axis scan of rat intestine were 56.0, 100.0, 77.3, 143.7, and 91.7 μm, respectively, and PEI-L-TA@MON displayed superiority in mucus penetration and penetrated deeper along the z-direction.

Mucosal adhesion and permeation of PEI-L/D-TA@MON

With respect to the superior mucus coverage and penetration of nanomedicines, we investigated the adhesion ability of nanomedicines on the intestinal mucosa via the elution method (Supplementary Fig. 40). Under washing with simulated intestinal fluid (SIF), the adhesion ratios of PEI@SiO_2, PEI-L-TA-@SiO_2, PEI-D-TA-@SiO_2, PEI-L-TA@MON, and PEI-D-TA@MON were 71.8%, 80.3%, 77.0%, 85.3%, and 79.7% at 1 min and 26.0%, 50.6%, 47.4%, 66.7%, and 49.6% at 5 min, respectively (Fig. 6e, Supplementary Fig. 40). Consistently, more PEI-L-TA@MON remained on the mucosa after elution followed by PEI-L-TA@SiO_2, as shown by the strong fluorescence intensities detected on the mucosa, indicating prominent chiral recognition and stereo-matching between the chiral nanostructures and the inherent chiral topologies of the biosurfaces (Fig. 6f, g). Similar phenomenon was noticed on the intestinal mucosa of humans and IBD rats, wherein the adhesion ratios of PEI-L-TA@MON were 3.0-, 1.1-, 1.6-, 1.2- and 3.1-, 1.1-, 1.5-, 1.3-folds higher than those of the other nanomedicines, respectively. The intestinal mucosa was then fixed and assessed using CLSM. As can be seen in Fig. 6h, nanomedicines permeated deeper into the intestinal mucosa of IBD rats than in healthy rats, because of the attenuated mucus and the injured mucosa in the inflammatory state. To be specific, PEI-L-TA@MON and PEI-D-TA@MON showed 1.1- and 1.2-folds higher penetration depths in the IBD intestinal mucosa than that in the healthy mucosa, respectively, and were highly accumulated on lesion sites with apparent mucosa injury and villi atrophy (Supplementary Fig. 41). Herein, the pathological mucosa with the specific expression of transferrin and eosinophilic cationic protein was positively charged and electrostatically attracted with the negatively charged ionized L/D-TA, thus providing a material basis for lesion locating and targeted delivery of these chiral nanomedicines[47,48].

To ensure the best use of PEI-L/D-TA@MON for intestinal disease therapy, we studied whether the improved bioadhesion of the nanomedicine would lead to the enhanced improved retention and penetration in the lesion location. Mice were orally administrated with RITC-labeled nanomedicines for 2 h, and the colon was excised for CLSM observation (Supplementary Fig. 42). As shown in Fig. 6i, j, in the transection of the colon of healthy mice, PEI@SiO_2 was mainly gathered in the center of the intestinal lumen rather than entering the villi, whereas PEI-L-TA@MON entered deeply along the intestinal wall. PEI-L/D-TA@MON could also penetrate through the ex vivo intestinal tubes of humans. Excitingly, in accordance with the mucus penetration and mucosal adhesion trends, nanomedicines effectively accumulated and permeated into the villi of the inflamed colon, implying good targeting ability (Fig. 6k, Supplementary Fig. 43).

Biological fate and biocompatibility of PEI-L/D-TA@MON

Subsequently, we inspected the GIT retention and biodistribution of nanomedicines via the IVIS Lumina Series III Living Image System. From the direct observation of fluorescence images, RITC labeled nanomedicines were found in the small intestine of healthy mice at 1 h post-oral administration, distributed in the large intestine at 2–6 h, and were excreted thereafter (Supplementary Figs. 43, 44). In contrast, nanomedicines exhibited improved accumulation in the colon of the IBD mice due to the increased intestinal permeability. Particularly, PEI-L/D-TA@MON was aggregated in the inflammatory colon for more than 24 h. In addition, all nanomedicines were mainly aggregated in the GIT without entering into the blood circulation and were barely distributed in the main organs, falling into the concept of targeted therapy and eliminating the potential safety hazards.

PEI-L/D-TA@MON displayed favorable hemocompatibility in the concentration range of 0–800 μg/mL (Supplementary Fig. 45). Subsequently, we performed a biocompatibility study of the nanomedicines through oral administration of PEI-L/D-TA@MON to mice for 14 days, after which the blood was collected for hematological and biochemical tests, and the GIT and major organs were removed for histopathological examinations. The nanomedicines showed favorable biocompatibility, with no death or significant weight loss, and the biomedical and hematological indexes fell within the reference values (Supplementary Figs. 46–48). HE staining of the heart, liver, spleen, lung, kidney, stomach, small intestine, and colon of mice confirmed that no histopathological abnormalities or damage occurred, indicating negligible toxicity or irritation of these nanomedicines (Supplementary Fig. 49–51). In addition, PEI-L/D-TA@MON caused no irritation once exposed to the human intestinal mucosa (Supplementary Fig. 52).

Taken together, PEI-L-TA@MON exhibiting large surface area, preferential chiral conformation, and specificity interaction with the positively charged inflammatory lesions could specifically accumulate on the colon to realize lesion localization, bringing benefits for treating intestinal diseases.

Prophylactic therapy of PEI-L/D-TA@MON on IBD mice

Given the promising results of PEI-L/D-TA@MON in scavenging the pathogenic factors, ameliorating the intracellular oxidative stress, and realizing lesion localization, PEI-L/D-TA@MON was orally administrated to mice for the therapy of IBD in vivo. Mice drunk water containing 3% DSS for 7 days to induce an acute IBD model (Fig. 7a). To protect mice from colitis, they were simultaneously orally

https://doi.org/10.1038/s41467-025-57890-8

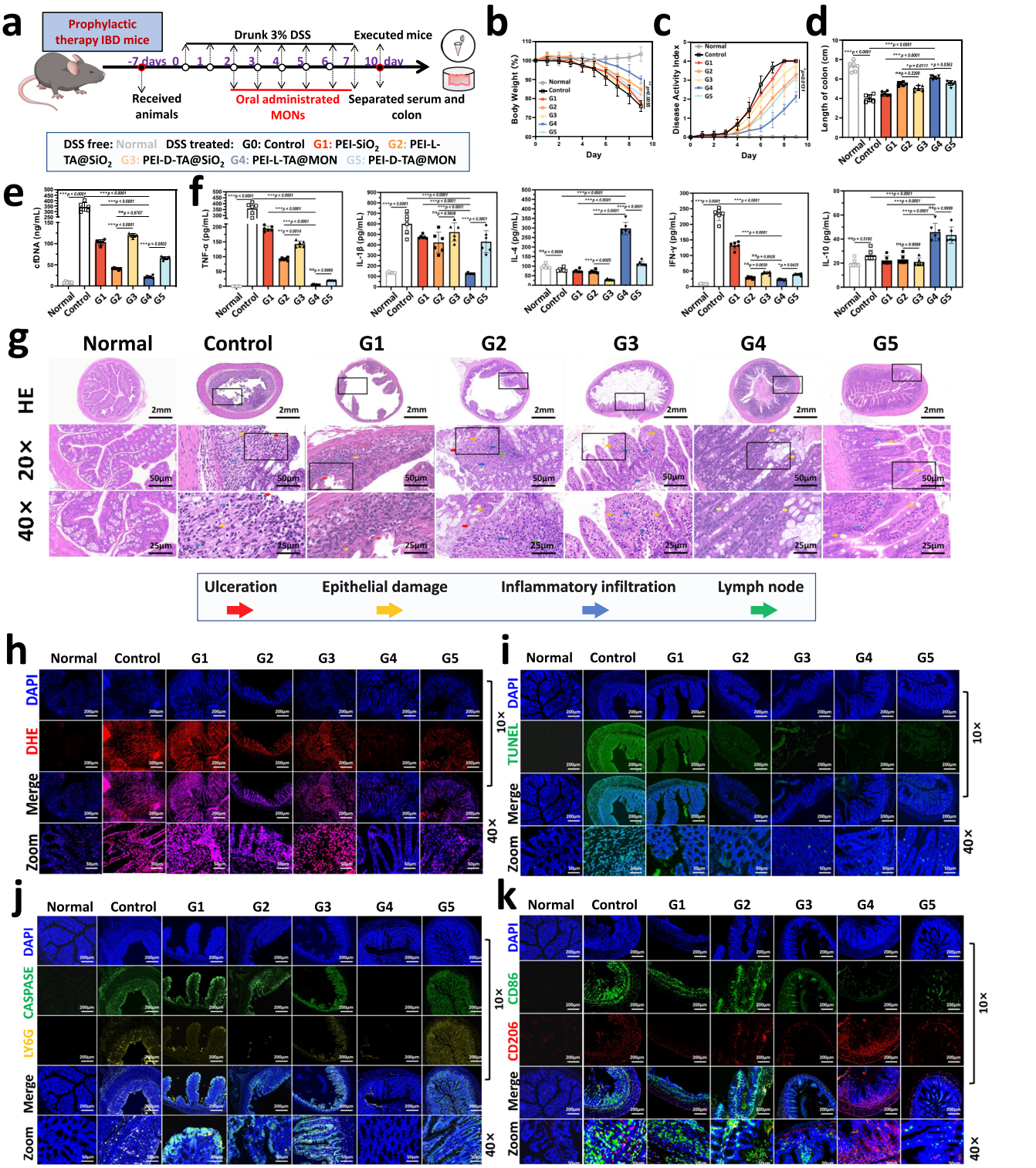

Fig. 7 | Prophylactic therapy of PEI-L/D-TA@MON on DSS-model mice. **a** Schematic illustration on the timeline of the model fabrication of DSS-induced colitis on mice and experimental procedures. For prophylactic therapy, PEI-L/D-TA@MON DSS-model mice were orally administered with saline (control), PEI@SiO_2 (G1), PEI-L-TA-@SiO_2 (G2), PEI-D-TA-@SiO_2 (G3), PEI-L-TA@MON (G4), and PEI-D-TA@MON (G5), respectively. **b** Daily body weight, **c** DAI, **d** colon length, **e** serum cfDNA levels, and (**f**) cytokine levels in homogenized colonic tissues of DSS-model mice treated with nanomedicines. $n = 6$ biologically independent animals. **g** HE staining, **h** DHE staining (blue: nucleus stained with DAPI, red: ROS), **i** Tunel staining (blue: nucleus stained with DAPI, green: apoptotic cells), **j** Caspase3 and Ly6G staining (blue: nucleus stained with DAPI, green: cell apoptosis, yellow: neutrophil), and (**k**) CD86 and CD260 staining (blue: nucleus stained with DAPI, green: M1 macrophage, red: M2 macrophage) of colon tissues from DSS-model mice treated with nanomedicines. n = 3 biologically independent animals. Data presented as the mean ± SD. $^{*}P < 0.05$ and $^{**}P < 0.01$ and $^{***}P < 0.001$ by two-tailed Student's t test. Source data are provided in the Source Data file.

administered with nanomedicines once daily from days 2 to 7, alongside a control group of IBD mice treated with saline and a normal group of healthy mice. As shown in Fig. 7b, c, mice without DSS treatment showed normal performances and steady body weight, whereas DSS-model mice in the control group experienced severe weight loss, with clinical symptoms of diarrhea and blood-stained stools. Clinical symptoms obviously improved after nanomedicines therapy, with a reduced weight loss from 100% to 77.2%, 84.7%, 77.8%, 89.8%, and 81.7% and a decreased daily disease activity index (DAI) from 4 to 4, 3.3, 3.8, 2.1 and 3.1 for PEI@SiO_2, PEI-L-TA-@SiO_2, PEI-D-TA-@SiO_2, PEI-L-TA@MON, and PEI-D-TA@MON, respectively (Fig. 7b, c, Supplementary Table 10). On day 10, we collected the blood and colon samples from mice for cfDNA detection, inflammatory cytokine determination, and HE, IF, and IHC staining. To intuitively reflect the severity of colitis, the colon length was measured, and a significantly shortened colon length was observed after DSS stimulation (Fig. 7d, Supplementary Fig. 53). The average colon lengths of mice in the untreated normal, DSS-treated control, and PEI@SiO_2, PEI-L-TA-@SiO_2, PEI-D-TA-@SiO_2, PEI-L-TA@MON, and PEI-D-TA@MON groups were 7.3, 4.0, 4.5, 5.5, 5.1, 6.2, and 5.6 cm, respectively, revealing the gradual alleviation of colon damage. Moreover, the serum cfDNA level was dramatically decreased with the nanomedicines therapy (Fig. 7e). The inflammatory cytokines in colon tissues were measured using enzyme-linked immunosorbent assay (ELISA). The results showed that PEI-L-TA@MON treatment restored intestinal homeostasis, reduced the levels of proinflammatory cytokines, including TNF-α, interleukin-1β (IL-1β), interleukin-6 (IL-6), interleukin-17 (IL-17), monocyte chemotactic protein 1 (MCP-1), interferon-γ (IFN-γ), and improved the levels of antiinflammatory cytokines (interleukin-4 [IL-4] and interleukin-10 [IL-10], Fig. 7f, Supplementary Fig. 54).

HE staining of the colon in the control group indicated typical histological abnormalities of IBD, including local mucosal ulceration, necrosis of epithelial cells, extensive disappearance of crypts, massive infiltration of inflammatory cells, and the presence of lymphoid follicles marked by the red, yellow, blue and green arrows, respectively (Fig. 7g). Nanomedicines exhibiting two (PEI@SiO_2) or three (PEI-L/D-TA-@SiO_2) functional moieties partly attenuated the damage. PEI-L-TA@MON rescued the mice from DSS injury as shown by the basically normal mucosal structure, with regular finger-like crypts, a small proportion of inflammatory cells, and no lymphoid follicle formation, with the histological score reduced from 3.7 to 0.7, elucidating its efficacy against colitis (Supplementary Fig. 54, Supplementary Table 11). IF and IHC studies were carried out to reveal the immune microenvironment and cellular phenotypes. In accordance with the excessive generation of ROS in the human colon, DHE staining suggested sharply raised ROS level with pronounced red fluorescent signals in mice colitis (Fig. 7h, Supplementary Fig. 55). However, the superoxide signal was reduced with PEI-L-TA@MON treatment, exhibiting a superior antioxidant effect. Meanwhile, the apoptosis of enterocytes induced by colitis injury was significantly alleviated in the PEI-L-TA@MON group (Fig. 7i). As markers associated with the functionality of tight junctions, the expression of zonula occludens-1 (ZO-1) and occludin were significantly downregulated in the colon tissue of colitis mice, whereas the expression of these two proteins basically returned to normal levels under PEI-L-TA@MON treatment, because of the restoration of the intestinal barrier (Supplementary Figs. 55, 56). The IF images of F4/80 and CD31 demonstrated the activation of monocytes/macrophages in IBD-model mice and the decrease in the number of endotheliocytes (Supplementary Figs. 55, 57). CD86 and CD206 staining was conducted to understand the roles of macrophages in directing host inflammatory and immune processes. For mice with colitis, the number of macrophages assigned to the proinflammatory M1 type was raised in the control groups, whereas macrophages started to transfer to the antiinflammatory M2 type with nanomedicines therapy (Fig. 7k). In the PEI-L-TA@MON group, the M2 type macrophages dominated the microenvironment. Next, the activities of Ly6G and MPO, as neutrophil markers, were measured, wherein distinct neutrophil infiltration was noticed in colon tissues of mice (Fig. 7j, Supplementary Figs. 55, 58). Meanwhile, cell apoptosis and activation of the NF-κB signal pathway associated with inflammation were elevated. As shown in Supplementary Fig. 58 and Fig. 7j the MPO, Ly6G, caspase-3, and NF-κB activities of the PEI-L-TA@MON group were similar to those of the untreated normal group and were significantly lower than the other colitis groups, illustrating an interception of the inflammatory cascade relevant to macrophages and neutrophils.

On DSS-model IBD mice, we also noticed an aberrant immune state, wherein Th1 responses significantly outweigh Th2 responses (Fig. 8a, b, Supplementary Figs. 59, 60). After PEI-L-TA@MON treatment, the intestinal inflammation was alleviated through the harmonization of Th1/Th2 balance. As can be seen in the IF images of CD4 and FOXP3, small amount of Treg cells were found after the treatment of PEI@SiO_2 and PEI-L/D-TA@SiO_2, which was further improved by PEI-L-TA@MON therapy (Fig. 8c). Th2 and Treg cells also increased in the spleens of mice after PEI-L-TA@MON treatment, further suggesting a subsiding inflammatory state (Fig. 8d, Supplementary Figs. 61, 62).

Transcriptomics analysis on the colon tissues of mice was conducted to reveal the therapeutic effect of PEI-L-TA@MON at the gene level. In comparison with the control group, PEI-L-TA@MON downregulated the expression of *Marco*, *Fpr1*, *Fpr2*, *F10*, *IL1a*, *Acod1*, *Mmp12*, *Cxcl2*, *IL18rap*, *IL10*, *IL1r2*, *Ctla4*, *Ptx3* genes and upregulated that of *Pkp1*, *Ccnb1*, *Ccnb2*, *Cdc20*, *Pif1*, *Nccrp1*, *Melk*, *Gp2*, *Brca1*, *Lrr1* genes. A differential gene cluster heatmap indicated that, PEI-L-TA@MON therapy significantly changed various gene levels in cellular processes, environmental information processing, and human diseases (Fig. 8e). Kyoto Encyclopedia of Genes and Genomes [KEGG] analysis highlighted the differential genes in the *P53*, *Tnf-α*, *Nf-κb*, T cell receptor signaling pathways and cytokine–cytokine receptor interactions, which were highly associated with the inflammatory cascade and the secretion of proinflammatory cytokines related to IBD progression (Fig. 8e, Supplementary Fig. 63).

Furthermore, the IHC images strongly confirmed the high expression of TLR4 and TLR9 in mice in the control group, which was induced by the enriched LPS and cfDNA in the inflammatory tissues (Fig. 8f, Supplementary Fig. 64). In the PEI-L-TA@MON group, the activation of immune cells was inhibited by reducing LPS- and cfDNA-induced TLR4/TLR9–MyD88–NF-κB signaling. Although we designed nanomedicines that specifically cleared LPS and cfDNA to prevent the activation of TLR4/TLR9, we found that the activations of Toll-like receptor-1 (TLR1)/Toll-like receptor-2 (TLR2)/TLR5 were also substantially inhibited, possibly due to the extensive adsorption effect of mesoporous silica structure and the improvement on the immune and microbial environments in the intestine (Supplementary Fig. 65). To verify the molecular mechanism, we isolated macrophages from the peritoneal fluid of mice and evaluated the protein content via western blotting (WB). After DSS induction, TLR4/TLR9–MyD88–NF-κB pathways were activated, which agreed with the pathophysiological process of IBD (Fig. 8g, Supplementary Fig. 66). The protein expression of TLR4, TLR9, MyD88, and NF-κB (p65) was activated in macrophages but was blocked after treatment with PEI-L-TA@MON. Collectively, PEI-L-TA@MON relieved oxidative stress, reduced inflammation, maintained immunity homeostasis, and restored the intestinal barrier.

Delayed therapy of PEI-L/D-TA@MON on IBD mice

We proceeded to explore the therapeutic effects of PEI-L/D-TA@MON against IBD with delayed treatment. Mice were given DSS for 7 days to induce colitis, received nanomedicines therapy from day 5 to day 11, and were sacrificed at day 14 (Fig. 9a). Equally unsurprisingly, mice in the control group exposed to DSS stimulation experienced the typical symptoms of IBD, including body weight loss (19.2%), mucous bloody

https://doi.org/10.1038/s41467-025-57890-8

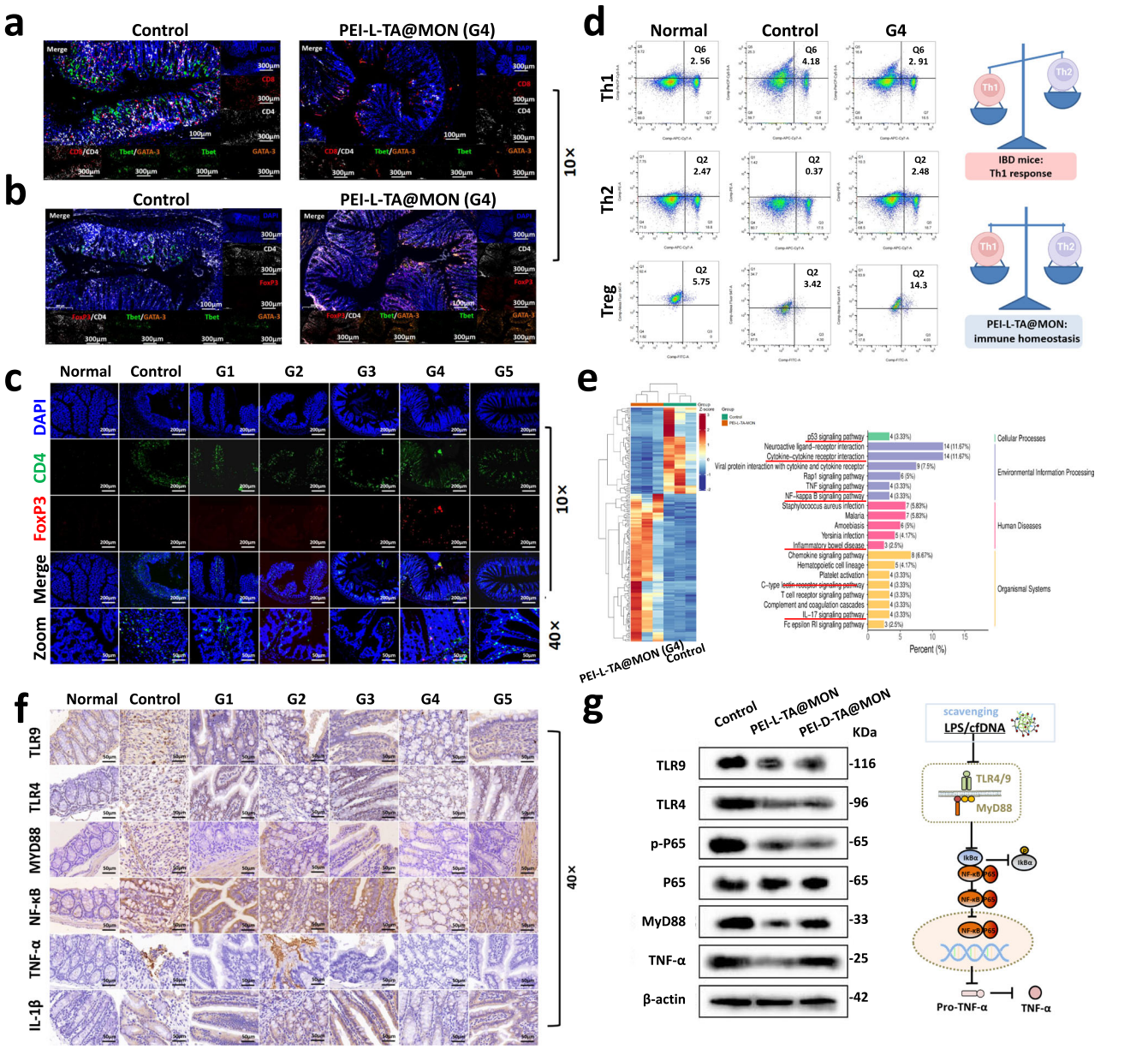

Fig. 8 | Prophylactic therapeutic mechanisms of PEI-L/D-TA@MON on DSS-model mice. a Multiplex IF staining on (**a**) T cells (blue: nucleus stained with DAPI, red: cytotoxic T cells marked with CD8 + , white: helper T cells marked with CD4+, green: Th1 cells marked with Tbet, orange: Th2 cells marked with GATA-3) and (**b**) CD4+ T cells (blue: nucleus stained with DAPI, white: helper T cells marked with CD4+, green: Th1 cells marked with Tbet, orange: Th2 cells marked with GATA-3, red: Treg cells stained with FoxP3) of colon tissues from DSS-model mice treated with PEI-L-TA@MON. **c** CD4 and FoxP3 of colon tissues from DSS-model mice treated with nanomedicines, blue: nucleus stained with DAPI, green: helper T cells marked with CD4+, red: Treg cells stained with FoxP3. **d** T cells analyzed using FCM from DSS-model mice treated with PEI-L-TA@MON. e Transcriptomics analysis (from left to right are DEGs clustering heat map and KEGG enrichment histogramof colon tissues of DSS-model mice after PEI-L-TA@MON treatment. **f** IHC staining (corresponding to TLR4, TLR9, MyD88, NF-κB, TNF-α and IL-1β, expressions). **g** WB analyses of TLR9, TLR4, MyD88, P65, P-65, TNF-α and IL-1β in peritoneal lavage fluid of DSS-model mice after PEI-L -TA@MON treatment. $n = 3$ biologically independent animals. Source data are provided in the Source Data file.

stool (DAI, 4), death (survival rate, 50%), and colon length shortening (from 6.9 to 3.4 cm), whereas PEI-L-TA@MON treatment effectively protected mice against DSS-induced acute IBD with remission on these clinical manifestations (Fig. 9b–d, Supplementary Figs. 67, 68). High cfDNA and proinflammatory cytokine levels were found in the model mice and were significantly reduced by PEI-L-TA@MON treatment (Fig. 9e, f, Supplementary Fig. 68). The histopathological examination on the colon tissues of IBD mice suggested severe intestinal wall ulcer, epithelial cell necrosis, and inflammatory cell infiltration, which could be repaired with the help of the nanomedicines (Fig. 9g). In the colon tissues of mice received PEI-L-TA@MON therapy, an intact mucosal structure with a very low percentage of inflammatory cells was observed, and assessed with a minimal disease score, elucidating its protective effect against IBD (Supplementary Fig. 68). Compared to mice in the control group, which exhibited potent oxidative stress and cell apoptosis, the PEI-L-TA@MON-treated mice displayed negligible ROS and apoptosis signals (Fig. 9h, i, Supplementary Fig. 69). Furthermore, the damaged intestinal barrier was basically remodeled to a normal condition as shown by the enriched expression of ZO-1, occludin, and CD31 (Supplementary Figs. 69–71). The activation of monocytes/macrophages and recruitment of neutrophils, as well as the promotion of inflammatory cascade, were toughly blocked, along

https://doi.org/10.1038/s41467-025-57890-8

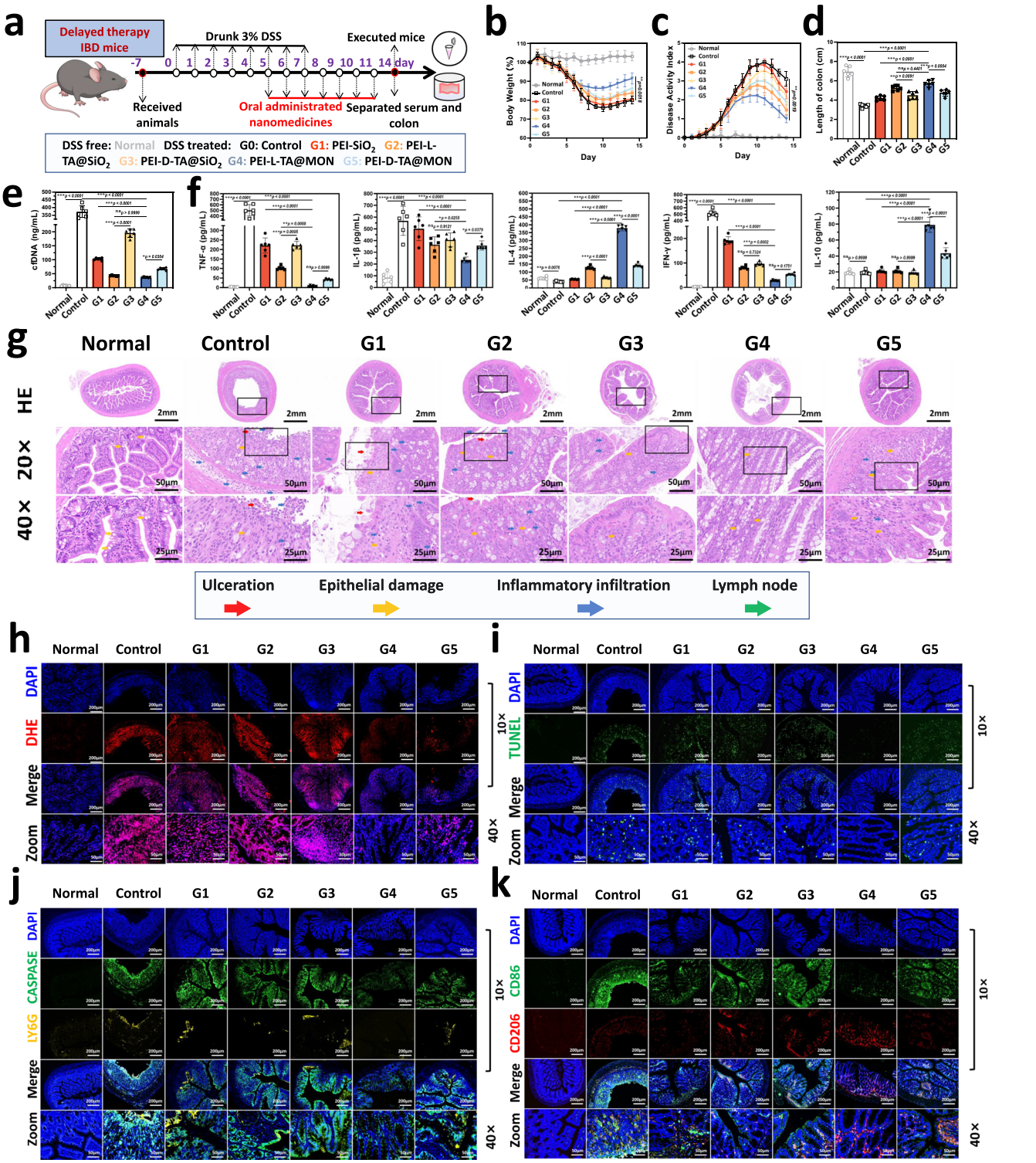

Fig. 9 | Delayed therapy of PEI-L/D-TA@MON on DSS-model mice. a Schematic illustration on the timeline of the model fabrication of DSS-induced colitis on mice and experimental procedures. For delayed therapy, PEI-L/D-TA@MON DSS-model mice were orally administered with saline (control), PEI@SiO_2 (G1), PEI-L-TA-@SiO_2 (G2), PEI-D-TA-@SiO_2 (G3), PEI-L-TA@MON (G4), and PEI-D-TA@MON (G5), respectively. **b** Daily body weight, (**c**) DAI, (**d**) colon length, (**e**) serum cfDNA levels, and (**f**) cytokine levels in homogenized colonic tissues of DSS-model mice treated with nanomedicines. $n = 6$ biologically independent animals. **g** HE staining, (**h**) DHE staining (blue: nucleus stained with DAPI, red: ROS), (**i**) Tunel staining (blue: nucleus stained with DAPI, green: apoptotic cells), (**j**) Caspase3 and Ly6G staining (blue: nucleus stained with DAPI, green: cell apoptosis, yellow: neutrophil), and (**k**) CD86 and CD260 staining (blue: nucleus stained with DAPI, green: M1 macrophage, red: M2 macrophage) of colon tissues from DSS-model mice treated with nanomedicines. $n = 3$ biologically independent animals. Data presented as the mean ± SD. $^*P < 0.05$ and $^{**}P < 0.01$ and $^{***}P < 0.001$ by two-tailed Student's t test. Source data are provided in the Source Data file.

with decreased F4/80, CD86, Ly6G, MPO, NF-κB, and caspase-3 activities (Fig. 9j, k, Supplementary Figs. 70, 72). The amount of Treg cells was improved after PEI-L-TA@MON treatment (Supplementary Fig. 73). IHC also identified the role of PEI-L-TA@MON in reducing cfDNA- and LPS-induced TLR4/TLR9–MyD88–NF-κB signaling (Supplementary Figs. 74, 75). Finally, we collected the feces from mice in each group for 16S rRNA sequencing analysis. As shown in Fig. 9n and Supplementary Fig. 76, PEI-L-TA@MON effectively regulated the gut microbiome in DSS-treated mice with a decrease in both community richness and composition, indicating its potential beneficial effects from a microbial perspective[49,50]. Taken together, the therapy of PEI-L-TA@MON against IBD, concerning cfDNA, ROS and LPS scavenging, GIT retention, and lesion targeting, substantially ameliorated oxidative stress, blocked the inflammatory cascade, repaired the intestinal barrier, remodeled the immune homeostasis, and achieved the best preventive and therapeutic effects against IBD.

Pharmaceutical properties of PEI-L/D-TA@MON

Employing a biosilicification-mimicking strategy, PEI-L/D-TA@MON was formed within seconds through a very simple mixing process of adding the inorganic/organic silica source to the PEI-L/D-TA solution. The synthesis was mild, easy operation and high yield (between 63.7% and 66.4%), illustrating the prominent efficiency of the catalytic template PEI-L/D-TA to promote the hydrolysis of alkoxysilane and silica deposition (Fig. 10a). It should be noticed that, the whole process was performed under neutral pH and ambient conditions, uninvolving

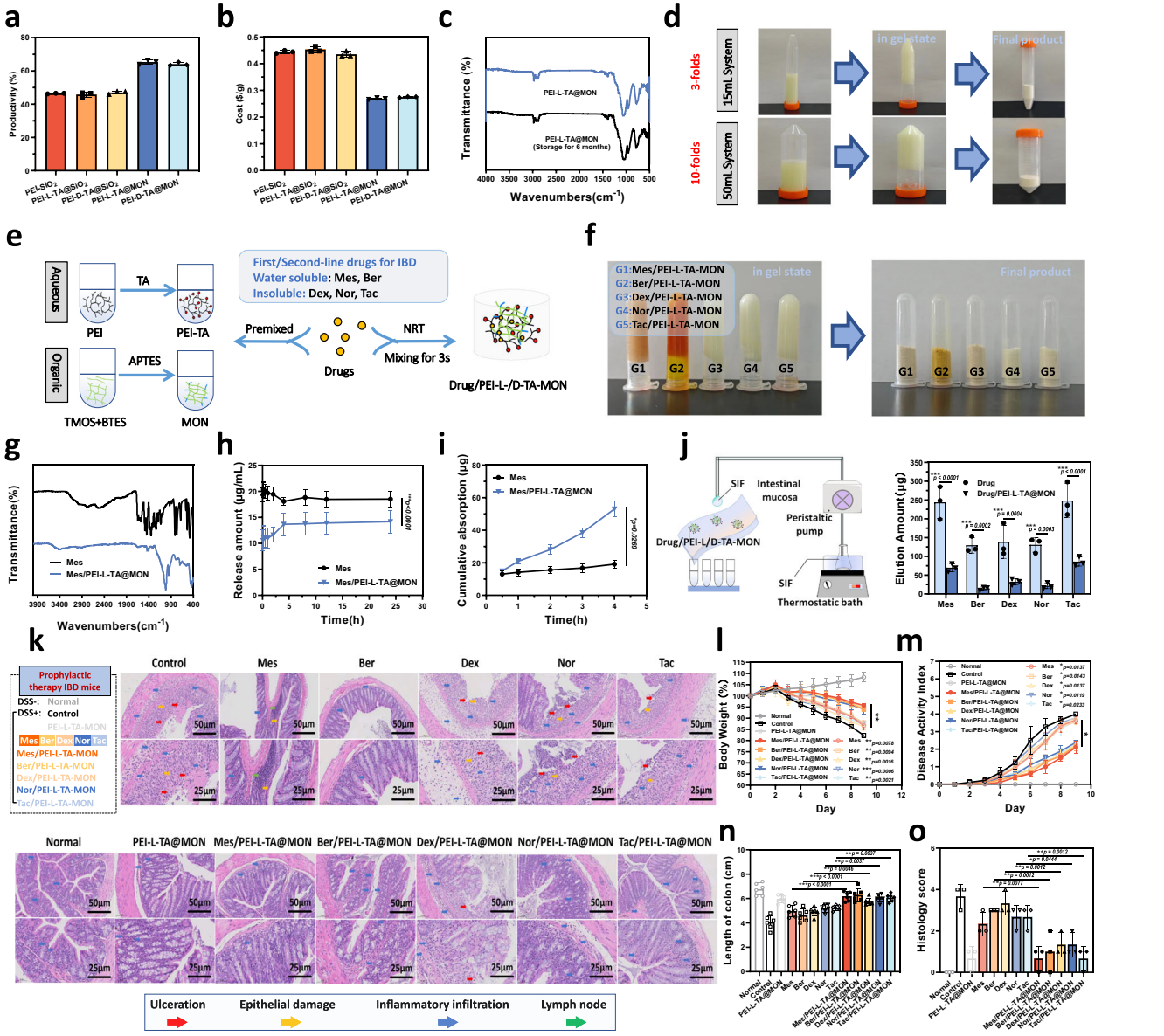

Fig. 10 | Pharmaceutical and synergistic therapy properties of PEI-L/D-TA@MON. a Yield ($n = 3$ independent experiments) and (**b**) raw material cost of nanomedicines ($n = 3$ independent experiments). **c** FTIR of PEI-L-TA@MON after store at room temperature for 6 months. **d** Appearances of 3- and 10-folds large-scale nanomedicines in different states. **e** Schematic illustration on fabrication of Drug/PEI-L/D-TA@MON. **f** Appearances of Drug/PEI-L/D-TA@MON in different states. **g** FTIR spectra, **h** in vitro drug release, and (**i**) ex vivo drug absorption (determined using everted intestinal sac models) of Mes before and after loaded into nanomedicines ($n = 3$ independent experiments). **j** Schematic illustration and intestinal adhesion capacities of drugs before and after loaded into PEI-L-TA@MON ($n = 3$ independent experiments). **k** Grouping of animal and HE staining of colon tissues from DSS-model mice treated with drug loaded nanomedicines. **l** Daily body weight, **m** DAI, **n** colon length, and (**o**) histology score of DSS-model mice treated with nanomedicines. $n = 6$ biologically independent animals. $n = 6$ biologically independent animals. Data presented as the mean ± SD. $^{*}P < 0.05$ and $^{**}P < 0.01$ and $^{***}P < 0.001$ by two-tailed Student's t test. Source data are provided in the Source Data file.

large-scale instruments and extra energies. Only an oven was used to accelerate drying. The cost of raw materials was calculated to be 0.44, 0.45, 0.44, 0.27, and 0.28 $/g for PEI@$SiO_2$, PEI-L-TA@$SiO_2$, PEI-D-TA@$SiO_2$, PEI-L-TA@MON, and PEI-D-TA@MON, respectively (Fig. 10b, Supplementary Table 12). To explore the possibility of an instrument- and energy-free process, PEI-L-TA@MON was left to naturally dry at room temperature, and was fully dried within 36 h (Supplementary Fig. 77). We also stored PEI-L-TA@MON in a cool and dry place at ambient temperature and pressure for 6 months, and examined the structure and functional groups via TEM, XPS and FTIR. As can be seen in Supplementary Fig. 78, complete aggregated NPs were observed without any obvious degradation. XPS and FTIR showed the presence of elements Si, O, N, C, and S, and the existence of Si–OH, Si–O–Si, S–S, and –NH– groups, without variation on the valence state, demonstrating the storage stability of PEI-L-TA@MON (Fig. 10c, Supplementary Fig. 79). We noticed that PEI-L-TA@MON was formed in situ in 5 mL tubes, and we then expanded the volume of the system to 3 and 10 folds, with proportional increases in the reactant amounts and solvent volumes (Fig. 10d). Excitingly, PEI-L-TA@MON successfully formed within a few seconds in both the 15 and 50 mL systems, creating a possibility for expanded production.

Drug delivery and synergistic therapy of PEI-L/D-TA@MON

Although we designed "drug-free" nanomedicines, the mesoporous structure of PEI-L/D-TA@MON maintained the drug-loading sites. Using a premixing strategy, drugs can be in situ loaded into PEI-L-TA@MON with high efficiency. Considering the feasibility of synergistic therapy, five first- or second-line drugs, including mesalazine (Mes), berberine hydrochloride (Ber), dexamethasone (Dex), norfloxacin (Nor), and tacrolimus (Tac) with anti-inflammatory, antidiarrheal, antibiosis, and immunomodulatory functions were predissolved in the aqueous or organic phases according to their solubility and formed the "drug-loaded" nanomedicines within seconds (Fig. 10e). As indicated in the FTIR and XRD results, drugs were highly dispersed and bound in the pore structure of PEI-L-TA@MON, along with the deprivation of crystallization (Fig. 10g, Supplementary Fig. 80). Conformance to the bio-adhesion of PEI-L-TA@MON, it also helped to improve the retention of loaded drugs for 1.3-1.7 times, increasing the intestinal drug content for local treatment, and benefiting the oral adsorption of drugs (Fig. 10j). Moreover, Mes/Ber/Dex/Nor/Tac-PEI-L-TA@MON showed sustained drug release manners (measured by the USP II paddle method using SIF as the release medium) and improved bioavailability (simulated through the everted intestinal sac method), and can therefore serve as a drug repository for sustained and targeted drug delivery (Fig. 10h, i, Supplementary Figs. 81, 82). By the way, it helped to improve drug stability by bounding into the system (Supplementary Fig. 83).

Finally, we studied the therapeutic effect of Mes/Ber/Dex/Nor/Tac-PEI-L-TA@MON on DSS-modeled mice (modeled according to the preventive therapy experimental methodology). As can be seen in Fig. 10l–n and Supplementary Fig. 84, mice treated with naked drugs could not completely alleviate the clinical symptoms, weight loss and colon length shortening. However, PEI-L-TA@MON as well as Mes/Ber/Dex/Nor/Tac-PEI-L-TA@MON treatment obviously protected the mice against DSS-induced IBD, including loss of body weight, shortening of colon length, and damage to colonic tissue. High proinflammatory cytokine levels were found in the DSS-model mice and mice treated with naked drugs, which could be significantly reduced by Mes/Ber/Dex/Nor/Tac-PEI-L-TA@MON treatment (Supplementary Fig. 85). HE staining discovered severe inflammatory cells infiltration on the circum-intestinal wall, crypts ectasia, ulcers formation, and goblet cells disappearances (Fig. 10k). After receiving naked drug therapy, inflammatory cell infiltration, ulcers formation, and goblet cells disappearances were still apparent, with a slightly decreased histological score from 3.7 to 2.3, 3.0, 3.3, 2.7, 2.7 for Mes, Ber, Dex, Nor, and Tac, respectively (Fig. 10o). In comparison, PEI-L-TA@MON as well as Mes/Ber/Dex/Nor/Tac-PEI-L-TA@MON showed almost no absence of crypts, goblet cells, or ulcers, with histological score within the range of 0-1.3, elucidating significant therapeutic effect against IBD. Best treatment came from Mes-PEI-L-TA@MON, which showed basically normal intestinal microstructure (histological score: 0). Based on the experimental results, we found that drug-containing nanomedicines worked significantly better than clinical drugs alone, and functioned approximatively or even better than chiral nanomedicines PEI-L-TA@MON due to the therapeutic effect of PEI-L-TA@MON as nanomedicine and the management on drug release, absorption and targeting by PEI-L-TA@MON. Undoubtedly, the facile conversions of PEI-L-TA@MON between "drug-free" and "drug-loaded" modes enabled synergistic therapy and rescued the possible defects of the chiral nanomedicine in IBD treatment, which provided flexible clinical protocols for patients and inspired alternative thinking for the development of nanomedicines.

Discussion

The cascade reaction of pathogenic factors, including LPS, cfDNA, and ROS, drives the occurrence and development of IBD. Simultaneously scavenging multiple pathogenic factors and achieving the lesion localization will bring substantial changes for IBD treatment. In this study, chiral nanomedicines PEI-L/D-TA@MON constructed by mimicking biosilicification strategy realized this conception. PEI-L/D-TA@MON included four functional moieties, including PEI, tetrathulfide bonds, mesoporous silica and L/D-TA, was formed within seconds under neutral pH and ambient conditions. Following oral administration, PEI-L/D-TA@MON efficiently stereoscopically matched with the mucosa to realize the long-term intestinal retention and anchored onto the positively charged damaged intestine for lesion targeting. In vitro and in vivo, PEI-L/D-TA@MON eliminated LPS, ROS, and cfDNA via adsorption, redox reaction, and electrostatic interaction, respectively, alleviating oxidative stress, inhibiting the inflammatory cascade, maintaining immune homeostasis, and blocking the vicious cycles of the disease to achieve efficient IBD therapy. Particularly, the facile conversion of PEI-L/D-TA@MON between "drug-free" and "drug-loaded" modes enabled synergistic therapy and provided flexible clinical protocols for IBD treatment. Experiments verified the low cost, rapid synthesis, instrument- and energy-free requirements, facile and scaled production, negligible toxicity and irritation, and satisfactory therapeutic effects of PEI-L/D-TA@MON, pathing significant research value and clinical translational prospects, and providing a reference for treating other inflammatory diseases as well as intestinal lesions.

Methods

Ethical statement

Our research complies with all relevant ethical regulations. All animal experiments were approved by the Animal Ethics Committee of China Medical University (Protocol Number: CMU20240642). Mice were maintained in a specific pathogen-free (SPF) environment according to the requirements of the Experimental Animal Ethics Committee of China Medical University.

The collection of patient data and samples was approved by the Ethics Committee of the China Medical University (Protocol Number: [2024]086, [2024]087). All participants provided written informed consent to donate their biological samples and information.

Animals and Cells culture

C57BL/6 mice (male, 6–8 weeks old, 20 g), and Sprague-Dawley (SD) rats (male, 6 weeks old, 200 g) were involved in the study, and received humane care. The animals were kept at ambient temperature with 12 h of alternating light and dark, were free to drink and eat and were adaptive fed for one week. Although we have used single-sex animals in

our research, we think that the research results were not only applicable to single sex.

RAW264.7 cells and Caco- 2 cells were purchased from the Procell Life Science Technology Co. Ltd (CL-0190 and CL-0005). RAW264.7 were cultured in DMEM medium containing 10% fetal bovine serum (FBS, procell) and 100 U/mL penicillin and 100 mg/mL streptomycinat 37 °C in a 5% CO_2 humidified incubator(Thermo Scientific™ BB 150, MA, USA). Caco-2 cells were cultured in DMEM with 1% non-essential amino acid, 20% FBS, 100 U/mL penicillin and 100 mg/mL streptomycin at the same conditions. All cell lines were validated using short tandem repeat (STR) markers and were tested negative for mycoplasma contamination.

Clinical data and samples from IBD Patients

We defined the disease stage of IBD patients based on the clinical criterions according to the medical records, wherein Improved Truelove and Witts scoring systems was used to define the severity of illness of UC patients, while Crohn's disease activity index (CDAI) was used to define the severity of illness of CD patients[51]. We determined the sex and/or gender of participants based on the record in medical records. The endoscopy and CTE images, as well as the lymphocyte subpopulation results of 12 UC and 12 CD patients were reviewed to explicit the tissue injury and immune imbalance caused by IBD. Serum was collected from 60 IBD (including 30 UC [21 male and 9 female] and 30 CD [18 male and 12 female]) patients and 30 healthy volunteers (16 male and 14 female) at the First Hospital of China Medical University.

Colon tissues were collected from 24 IBD patients (12 UC [6 male and 6 female] and 12 CD [8 male and 4 female]), and subjected to HE staining to observe pathological changes. IHC staining was carried out to detect the expressions of TNF-α, IL-1β, TLR4, TLR9, MyD88, and NF-κB. We also carried out DCFH and Tunel staining to detect the levels of ROS and apoptosis, multiplex IF staining for MPO, CD31, CD68, CD86 and CD260, for CD8/CD4/Tbet/GATA-3, and for CD4/Tbet/GATA-3/FoxP3 to indicate the immune microenvironments. Paraneoplastic tissues were obtained from 13 bowel cancer patients (8 male and 5 female) received tumorectomy to study the intestinal permeability of nanomedicines.

Materials

Branched PEI (M.W.20000) and TMOS were purchased from Xiya Reagent (Chengdu, China). L-/D-TA were bought from Adamas-beta (Shanghai) Chemical Reagent Co., Ltd (Shanghai, China). BTES and APTES were purchased from Shanghai Rhawn Chemical Technology Co., Ltd (Shanghai, China). FITC and RITC were provided by Beijing Bailingwei Technology Co., Ltd. (Beijing, China). Mes, Ber, Dex, Nor and Tac were purchased from Beijing Huawei Ruike Chemical Technology Co., Ltd. (Beijing, China).

Software part

The software used for data collection in this study including AppCI-Main_X800; OMNIC 7.3; Avantage v6.6.0; Zetasizer Software 7.13; Tecan i-control 2.0.10.0; Indigo 2.0.5.0; Slideviewer 2.5; BD Accuri C6 Plus Software 1.0.23.1; HISAT 2.2.2; DeSeq2 1.38.3; ClusterProfiler 4.6.0. The software used for data analysis including GraphPad Prism 9.5.0; ImageJ 1.54 f; Ri386 3.2.3; Microsoft Office 2016; FlowJo 10.8.1.

Single-cell sequencing

Single-cell sequencing datasets (GSE214695 and GSE215001) obtained from the Gene Expression Omnibus database (https://www.ncbi.nlm.nih.gov/geo/) was involved in this study. GSE214695 was identified as single-cell RNA sequencing data from 6 UC patients and 6 healthy individuals, with the total cell count of 37433 (UC17082 + HC20351). GSE215001 include the total cell count of 29687 came from 3 CD patients and 2 healthy individuals. We first conducted quality control on the sequencing data by removing cells expressing fewer than 300 or larger than 5000. The 25% mitochondrial ratio gene in cells was also set as a filtering threshold. Then, we applied the LogNormalize for normalization to extract genes with large inter-cell variation coefficients, used principal component analysis (PCA) for dimensionality reduction, and employed FindNeighbors and FindCluster to get the cell clusters. The single-cell data was annotated with known cell markers, wherein a double-check strategy was applied by comparing the marker genes with the public Cellmaker (CellMarker2.0) database and meanwhile directly visualizing the marker genes from the literature source to check cell identity.

Determination of pathogenic factors in the serum of IBD Patients

In a typical run, 100 μL serum was added to a 96-well plate. Subsequently, 100 μL the aqueous working solution of the Quant-iT™ PicoGreen™ dsDNA Reagent was added to each sample and incubated for 5 min at room temperature. The fluorescence intensity was measured at 485 nm excitation and 520 nm emission. High-range standard curves (10 ng/mL-1 μg/mL) and low-range standard curves (250 pg/mL-25 ng/mL) were set up separately, and the cfDNA concentration was calculated from the standard curves. Human LPS (lipopolysaccharide) ELISA kit (Andy Gene, Beijing, China) was used to detect LPS in the serum of healthy individuals and patients. 40 μL sample diluent and 10 μL serum (diluted five times) were added to the enzyme-coated plate, sealed at 37 °C and incubated for 30 min. Then 50 μL enzyme reagent was added, and the plate was incubated for 30 min at 37 °C. After washing, 50 μL color developer A and 50 μL developer B were added and mixed gently. The color was protected from light at 37 °C for 15 min. The reaction was terminated by adding the termination solution and the OD value was measured at 450 nm. The LPS concentration was calculated from the standard curve. Hydrogen Peroxide (H_2O_2) Colorimetric Assay Kit (Elabscience, Wuhan) was used to detect H_2O_2 concentration in the serum of healthy individuals and patients. 100 μL buffer solution was added to the measurement wells and preheated at 37 °C for 10 min. 15 μL serum and 100 μL ammonium molybdate reagent were subsequently added. The OD value of each well was measured at 405 nm by shaking for 5 s and standing for 10 min. H_2O_2 concentration was calculated from the standard curve.

Preparation of PEI-L/D-TA@MON

PEI-L/D-TA agglutination solution (10 mg/mL) was prepared by adding 0.4 g and 0.38 g L-TA or D-TA to 40 mL deionized water. Then 1 mL PEI-L-/D-TA agglutination solution was added into 5 mL EP tube, followed by the addition of 3 mL organic/inorganic silica source solution (1 mL TMOS mixed with 1 BTES and 1 mL ethanol) and 0.1 mL APTES. After mixing, the system was stood statically, and the gelling time was recorded. PEI-L/D-TA@MON was obtained after drying and grinding.

For comparative study, nanomedicines exhibiting two or three functional moieties were also synthesized. To be specific, PEI-L-/D-TA-@SiO_2 was prepared by the same procedure except that 2 mL TMOS ethanol solution was used instead of organic/inorganic silica source solution. On this basis, PEI@SiO_2 was formed by using PEI agglutination as template without the existence of L-/D-TA.

Characterization of PEI-L-/D-TA@MON

The morphologies of the nanomedicines were observed by TEM (Thermo Scientific, Talos F200X, USA) and SEM (Thermo Scientific, Verios 5UC, USA). Before TEM examination, the nanomedicines were dispersed in ethanol under ultrasound and deposited on carbon-coated copper grids with porous carbon films. The distribution of elements on PEI-L-TA@MON was acquired by EDS mapping. FTIR spectra of the agglutination solution and the nanomedicines were measured with an infrared spectrophotometer (Spectrum 1000, Perlmer, USA) at 400–4000 cm^{-1}. The zeta potential of the agglutination

solution and the nanomedicines dispersed in deionized water were investigated by a Zetasizer Lab analyzer (Malvern, Britain). The contents of C, N, O, Si, and S elements MONs were analyzed by an XPS instrument (ESCALAB 250Xi spectrometer, Thermo Fisher Scientific, USA). The pore characteristics of nanomedicines were obtained by the nitrogen adsorption/desorption tests with a nitrogen adsorption analyzer (VSorb 2800 P, app-one, China). The S_{BET} and average pore size (V_t) of PEI-L-/D-TA@MON were calculated by Brunauer–Emmett–Teller (BET) and Barrett–Joyner–Halenda (BJH) methods, respectively. TGA was carried out via a microcomputer differential thermal analysis instrument (HCT-1, Beijing, China) using air as a carrier gas from 25 to 700 °C. Moreover, PEI-L-/D-TA@MON were subjected to the SAXD and XRD analysis with nickel filtration of Cu-Ka radiation on an X-ray diffractometer (transparent, Netherlands) at the angles (2θ) of 0.5–10° and 5–50°, respectively. The CD spectra of the agglutination solution and the nanomedicines were studied by a CD apparatus (MOS-500, Bio-Logic, France) to confirm their chirality.

Preparation of RITC-PEI-L-/D-TA@MON

RITC-APTES was prepared by adding 100 μL APTES to the ethanol solution of RITC (50 mg/mL) and stirring vigorously for 24 h under dark conditions. Subsequently, 100 mg nanomedicine was dispersed in 2 mL ethanol under ultrasonication, mixed with 100 μL of RITC-APTES solution for 24 h, repeated washed with ethanol, and dried to obtain RITC-PEI-L-/D-TA@MON.

To study the fluorescence stability of nanomedicines, RITC-PEI-L-/D-TA@MON was dispersed in SIF, SIF containing 5 mM GSH, SIF containing 2 mM H_2O_2, or SIF containing 10 mM H_2O_2. After 0, 2, 6, and 12 h incubation, the fluorescence spectra of the system were recorded by microplate reader. Finally, the supernatant was collected by centrifuged, and subjected to fluorescence detection, wherein the above mediums were used as controls.

Surface/interface properties of PEI-L-/D-TA@MON

The wettability of the nanomedicines was evaluated by measuring the contact angles between the solid/liquid interfaces. PEI-L-/D-TA@MON (50 mg, $n = 3$) was compressed into a tablet and exposed to a drop of SIF. The contact angles were determined at the preset time intervals using a contact angle meter (JCY, Fangrui, China), equipped with a high-resolution camera to capture the image sequences. Furthermore, to assess its potential for chiral recognition and ROS sensibility, H_2O_2 (2 mM) were added to SIF in contact with PEI-L-/D-TA@MON, thereby simulating the interfacial interactions between nanomedicines and the medium in varying microenvironments.

The oil-water partition coefficient (lgP_{ow}) of PEI-L-/D-TA@MON was investigated utilizing the shake flask method. 100 mL n-octanol and 300 mL distilled water were mixed in a shaker at 30 °C for 24 h to achieve saturation. The two phases were separated by standing and layering in a dispensing funnel. Subsequently, 1 mL RITC-PEI-L-/D-TA@MON ($n = 3$) were dispersed in n-octanol-saturated distilled, followed by the addition of 4 mL water-saturated n-octanol, vortexed for 3 min, and shaken at 30 °C for 1 h. The fluorescence signals in the aqueous and organic phases were measured separately, and the lgP_{ow} values of the PEI-L-/D-TA@MON were calculated in accordance with the following equations:

$$\lg P_{ow} = \lg \frac{F_0}{F_w} \tag{1}$$

where F_0 and F_w are the equilibrium fluorescence intensity of the PEI-L-/D-TA@MON in n-octanol and in the aqueous phase, respectively.

Adsorption model onto PEI-L-/D-TA@MON

The adsorption between nanomedicines and various pathogenic factors were primarily analyzed by MD simulation. Firstly, the molecular models of pathogenic factors, including H_2O_2, lipid A, nucleotide, L-Ala and D-Ala, were formed using a Materials Studio (MS) software and sent to geometry optimization optimal and electrostatic potential analysis by DMol3 module. Meanwhile, molecular models of PEI and L-TA or D-TA chain were combined into PEI-L/D-TA, and mixed silica source models was built according to the polycondensation mechanism between TMOS, BTES and APTES. PEI-L-/D-TA was assemble into a frame, wherein the mixed silica source was inlaid onto the scaffold to obtain the PEI-L-/D-TA@MON model with a sheet structure. These pathogenic factors were regarded as adsorbents, respectively uniformly placed on both sides of PEI-L-/D-TA@MON model, and allowed to adsorb by PEI-L-/D-TA@MON via MD simulation to obtain the equilibrium configuration, wherein the ensemble was NVT, simulation temperature was 25°C, simulation duration was 1 fs, and the total simulation time was 5000 ps. After equilibrium, the binding energy E_{int} between the nanomedicines and the pathogenic factors can be calculated as follows:

$$E_{int} = E_{M+PEI-L-/D-TA@MON} - \left(E_M + E_{PEI-L-/D-TA@MON}\right) \tag{2}$$

where $E_{M+PEI-L-/D-TA@MON}$, E_M and $E_{PEI-L-/D-TA@MON}$ represent the average energy of the adsorption system, the pathogenic factors and the nanomedicines, respectively.

In vitro assay of cfDNA- and LPS scavenging capacity

Nanomedicines were first used to adsorb the dyes RhB and EB. Nanomedicines (20 mg, $n = 3$) were added to RhB or EB solution (0.02 mg/mL) with stirring. At the pre-determined time point, the supernatant was taken and measured the absorbance on a microplate reader at 554 and 611 nm, respectively.

L/D-Ala was selected as the representative chiral substances to investigate the chiral recognition tendency of the nanomedicines. 5 mg nanomedicines ($n = 3$) were exposed to 5 mL L/D-Ala solution (30 μg/mL) at 37 °C. After 24 h, 1 mL supernatant was extracted and combined with 1 mL acetate buffer (pH=5.4) and 1 mL ninhydrin solution. After heating at 100 °C for 20 min, cooling down to room temperature, and diluting with 3 mL of 60% ethanol, the adsorption amount was calculated by measuring the absorbance at 570 nm.

Subsequently, the DNA binding capacity of the nanomedicines was assayed by Quant-iT™ PicoGreen™ dsDNA Assay Kit (Fisher Scientific, USA). 5 mL ct-DNA (10 μg/mL, Sigma-Aldrich, USA) and 5 mL nanomedicines pH 7.4 PBS suspension (5 mg/mL, $n = 3$) were mixed evenly and separated the supernatant at the pre-determined time points. 100 μL PicoGreen working solution was added and the fluorescence intensity was measured at 485 nm excitation and 520 nm emission. The ct-DNA concentration was calculated from the standard curve.

The LPS adsorption capacity of the nanomedicines was assayed by a LPS ELISA Kit (Andy Gene, Beijing). In a typical run, 5 mL of LPS (240 ng/L, Solarbio, Beijing) were incubated with pH 7.4 PBS suspension (5 mg/mL, $n = 3$). At the pre-determined time points, 100 μL supernatant was separated by centrifugation and operated according to the instruction of test kits, and the OD value was measured at 450 nm. The LPS concentration was calculated from the standard curve.

In vitro antioxidant assay

The total radical scavenging capacity of the nanomedicines was determined using DPPH (Sigma-Aldrich, USA) strategy. 2 mL ethanol solution of nanomedicines (0, 1, 2, 4, 6, 8 and 10 mg/mL, $n = 3$) and 2 mL DPPH· solution (100 μg/mL) were mixed and kept in a dark place. After 0.5, 1, 2, 3 and 4 h, the OD value of the supernatant was detected at 520 nm.

Besides, ABTS and horseradish peroxidase (HRP) were used to react with the remaining H_2O_2. Specifically, 500 μL H_2O_2 (0.1 mM) was

co-incubated with 500 μL pH 7.4 PBS suspension of PEI-L/D-TA@MON (0, 2.5, 5, 10, 15, 20, 25 mg/mL, $n = 3$) at 37 °C and 100 rpm for 24 h, followed by the addition of 100 μL HRP (0.1 mg/mL) and 100 uL ABTS (1 mg/mL), resulting in the emergence of blue-green color. The UV absorbance was recorded at 415 nm using a multifunctional microplate reader. TMB (which is oxidized in the presence of peroxide and undergoes a discolouration reaction to produce a blue-green ionic polymer) method was used to determine the catalytic activity of PEI-L/D-TA@MON towards H_2O_2. Nanomedicines (1 mg/mL, $n = 3$), H_2O_2 (30%, 20 μL) and TMB (10 mg/mL) were mixed in the HAc/NaAc buffer (0.1 M, pH=3.6), react for 2 h. and measured the absorbance 652 nm.

The $\cdot O_2^-$ elimination capacity of nanomedicines was assayed by the Inhibition And Production Of Superoxide Anionic Colorimetric Assay Kit (Elabscience, Wuhan). WST-1 reacts with the superoxide anion generated by the xanthine and xanthine oxidase reaction system to produce a water-soluble formazan dye, which can be inhibited by the presence of the superoxide anion free radical inhibitor in the sample. Briefly, 20 μL pH 7.4 PBS suspension of PEI-L-TA@MON ($n = 3$) at different concentrations, 20 μL enzyme working solution and 200 μL substrate application solution were added to the wells, incubated at 37 °C for 20 min, and the OD value was measured at 450 nm by a microplate readers. The ·OH elimination capacity of nanomedicines was evaluated by Hydroxyl Free Radical Scavenging Capacity Assay Kit (Elabscience, Wuhan). H_2O_2/Fe^{2+} generates hydroxyl radicals via the Fenton reaction, and salicylic acid effectively captures the generated hydroxyl radicals and reacts to form the colored substance 2,3-dihydroxybenzoic acid. 100 μL substrate A, 100 μL substrate B, 480 μL distilled water, 200 μL substrate C and 20 μL PEI-L-TA@MON ($n = 3$) at different concentrations were added to a tube, mixed and incubated at 37 °C for 20 min, and measured the OD value at the wavelength of 510 nm. The H_2O_2 elimination capacity of nanomedicines was assayed by H_2O_2 Colorimetric Assay Kit (Elabscience, Wuhan). H_2O_2 reacts with ammonium molybdate to form a stable yellow complex. 500 μL H_2O_2 (0.1 mM) was co-incubated with 500 μL PEI-L-TA@MON ($n = 3$) at different concentrations at 37 °C and 100 rpm for 24 h. After a standard operation, the OD value of each well was measured at 405 nm by shaking for 5 s and standing for 10 min. H_2O_2 concentration was calculated from the standard curve.

EPR analysis

The scavenging ability of chiral nanomedicines on hydroxyl radicals and superoxide anions was evaluated on a Bruker EMXPlus spectrometer using EPR analysis. Fenton reaction was used to generate ·OH, which was generated by mixing 1.0 mM ferrous sulfate and 5 mM hydrogen peroxide at pH=4. The EPR spectra of DMPO/·OH were recorded after incubating the newly generated ·OH, DMPO and PEI-L-TA@MON (10 mg/mL, 100 μL) for 2 min at 37 °C. The scavenging rate was calculated from the signal intensity and the analysis was repeated three times.

Superoxide anion was generated by the reaction system of xanthine (0.5 mM) and xanthine oxidase (0.2 mU), and the EPR spectra of DMPO/$\cdot O_2^-$ were recorded after incubation of the newly generated superoxide anion, DMPO, and PEI-L-TA@MON (10 mg/mL, 100 μL) at 37 °C for 2 min. The scavenging rate was calculated from the signal intensity and the analysis was repeated three times.

Degradation tendency of PEI-L-/D-TA@MON

The stability and degradation trend of the nanomedicines were evaluated using weight loss method. PEI-L-/D-TA@MON ($n = 3$) was accurately weighed into tubes, wherein simulated gastric fluid (SGF), SIF, simulated body fluid (SBF), SIF containing 5 mM GSH, and SIF containing 2 mM H_2O_2 were separately added to make a solid concentration of 1 mg/mL. Under incubation at 37 °C and 100 rpm, the residual carriers were separated by centrifugation at a pre-determined time point, washed gently with water, dried, and weighed to determine the degradation trend. The degradation ratio was calculated as follows:

$$Degradation\ ratio\% = \frac{W_0 - W_t}{W_0} \times 100 \quad (3)$$

where W_0 is the initial weight of the MONs and W_t is the weight of the residue.

Cytotoxicity assay in vitro

RAW264.7 and Caco-2 cells were inoculated into 96-well plates at 10^4 and 5×10^3 per well ($n = 3$), respectively, and incubated under growth conditions at 37 °C and 5% CO_2. The original medium was removed, and then different concentrations of nanomedicines (ranged 0–80 μg/mL) were added and incubated for 12 h. The original medium was removed and replaced by the CCK-8 (Glpbio, USA) working solution. The OD value at 450 nm was measured using an enzyme marker and the proliferation viability of the cells was calculated by the following formula.

$$\text{Cell viability}(\%) = \frac{A_e}{A_c} \times 100\% \quad (4)$$

where A_e is the absorbance of the experimental group. A_c is the absorbance of the control group.

Cellular uptake capacity assay

RAW264.7 and Caco-2 cells were inoculated into 24-well plates (5×10^4 per and 10^5 per well, respectively, $n = 3$) and incubated at 37°C with 5% CO_2 for 12 h. Then, RITC labeled nanomedicines (0.25 mg/ml) were added. After 4 h incubation at 37 °C, the culture solution was removed and cells were washed three times with PBS. Subsequently, 4% paraformaldehyde was added for 15 min incubation. After washing with PBS, DAPI (Beyotime, Shanghai) was added and incubated for 10 min, washed and qualitatively observed by Nikon $C2^+$ Confocal microscope (Nikon Instruments Co.,Ltd., Shanghai). Meanwhile, FCM was used to quantitatively analyze the cellular internalization. RAW264.7 and Caco-2 cells were inoculated into 6-well plates (5×10^5 per well, n = 3) and incubated at 37 °C with 5% CO_2 for 12 h. Subsequently, the same operation was performed as in the confocal method. The fluorescence intensity of each well was detected by BD FACSCelesta™ Cell Analyzer (BD Biosciences, Franklin Lake, New Jersey, USA), and the cellular uptake of the series of carriers was quantitatively analyzed.

Intracellular antioxidant and anti-inflammatory assay

Firstly, CCK-8 method was used to examine the protective effect of nanomedicines on H_2O_2/LPS-induced oxidative stress-damaged cells. After the inoculation of RAW 264.7 cells ($n = 3$), H_2O_2 (final concentration of 200 μM, Sigma-Aldrich, USA) or LPS (final concentration of 20 μg/ml, Sigma-Aldrich, USA) were added into positive control and experimental groups, and the negative control group was given DMEM (Gbico, USA) medium treatment and incubated for a total of 12 h. Finally, the cell viability was determined and calculated.

IF and FCM were also used to examine the inhibition of ROS production within RAW 264.7, wherein LPS was administered to induce oxidative stress. Cells were inoculated in 24-well plates (10^5 per well, $n = 3$) and incubated at 37°C under 5% CO_2 growth conditions for 12 h. Medium containing nanomedicines (60 μg/mL) was added and incubated for 4 h, and then treated with LPS (final concentration of 20 μg/mL) for 4 h. The negative control was treated with DMEM medium. The original medium was removed, washed twice with PBS, and the cells in different treatment groups were stained with 10 μM DCFH-DA (Dalian Meilun Biotechnology Co., China) for 30 min. Fluorescence images were obtained by CLSM to analyze the presence of ROS. In addition, cells were inoculated in 6-well plates (5×10^5 per well, $n = 3$), incubated for 12 h, treated with nanomedicines (60 ag/mL) for 4 h, exposed to

LPS (final concentration of 20 PS/mL) for 4 h, and incubated for another 4 h. Then cells were stained with 10 μM DCFH-DA for 30 min and sent to FCM to quantitatively study the content of intracellular ROS using FlowJo V.10 software.

Live-dead cell staining was conducted to study the protective effect of nanomedicines against LPS-induced oxidative damage. RAW 264.7 was inoculated in 24-well plates (10^5 per well, $n = 3$) and incubated at 37 °C with 5% CO_2 for 12 h. Subsequently, control wells were added with nanomedicines (60 μg/mL) and incubated for 4 h. Cells in positive control and experimental groups were treated with LPS (final concentration of 20 μg/mL), while cells in negative control group were given DMEM medium and continued to be incubated for 4 h. The original medium was removed, washed twice with PBS, and treated accordingly using a live-dead cell kit (Shanghai Beyotime Biotechnology Co., China). Finally, fluorescence images were obtained by CLSM.

RAW 264.7 cells were inoculated in T25 culture flasks and cultured at 37 °C and 5% CO_2 under growth conditions for 12 h. Cells were treated with nanomedicines (60 μg/mL, $n = 3$) for 12 h, followed by stimulation with LPS (final concentration of 20 μg/mL) for 6 h. Cells in the negative control group were given DMEM medium treatment. Subsequently, the cells in each group were lysed and analyzed for SOD and CAT-like enzyme activities by SOD and CAT kits (Solarbio, Beijing).

The anti-inflammatory effect of nanomedicines against LPS was examined by measuring the TNF-α content in the cell supernatant. Cells were inoculated in T25 culture flasks and cultured at 37 °C and 5% CO_2 under growth conditions for 12 h. Following treating with nanomedicines (60 μg/mL, $n = 3$) for 12 h, cells were exposed to LPS (final concentration of 20 μg/mL) for 6 h. The cells in the negative control group were given DMEM medium. Subsequently, the cell supernatants were collected and the TNF-α levels in the supernatants of each group were assessed by ELISA kit (Elabscience, Wuhan).

Intestinal mucus penetration

Firstly, considering the viscoelastic characteristic of mucus, a series of mediums, including 0.5% HEC, 80% Gly, Gly containing L-Ala (0.5 mg/mL), Gly containing H_2O_2, (0.1Mm), fresh rat and human mucus were prepared. 1.5 mL medium was filled in a syringe, wherein 0.5 mL SIF suspension of RITC@PEI-L/D-TA@MON (1 mg/mL, $n = 3$) was slowly added to the upper layer of the medium and freely diffused into the mediums. Photos were taken and recorded after 6 h, followed by the separation of 0.2 mL sample from the bottom of the tube. After carefully washing, the fluorescence intensity was recorded (Ex/Em: 550/620 nm), and the particle penetration ratio was acquired as

$$\mathrm{Particlepenetrationratio}(\%) = \frac{I_i}{\sum_{i=1}^{5} I_i} \times 100 \quad (5)$$

where I_i denotes the fluorescence intensity of the nanomedicines escaped medium per 2 mL from bottom to top.

CLSM was applied to explore the mucus permeability of the nanomedicines. Freshly isolated colon from rats and DSS-model rats (drunk 4% DSS for 7 days) were gently rinsed with SIF, cut into 4 cm segments, ligated at both ends, injected with 500 μL FITC solution (10 μg/mL) and incubated in Tyrode solution at 37 °C for 10 min. 100 μL SIF suspension of RITC@PEI-L/D-TA@MON (100 μg/mL, $n = 3$) was injected after discarding FITC solution and incubated at 37 °C for 30 min. Colons were cut along the midline gently, washed with SIF and laid flat on a confocal dish (intestinal lumen side down). Finally, CLSM (THUNDER Image DMi8, Leica, Germany) images were photographed in z-stack mode.

RITC@PEI-L/D-TA@MON was penetrated along isolated ex vivo human intestine. Human intestinal segments were incubated first with 5 mL FITC-SIF solution (10 μg/mL) and then replaced by 1 mL SIF suspension of RITC@PEI-L/D-TA@MON (100 μg/mL, $n = 3$).

Multiple particles tracking

A multiparticle tracking technique was employed to observe Brownian trajectories of nanomedicines in intestinal mucus. Fresh mucus (200 μL) was carefully isolated from the lumen of rats, DSS-model rats and human intestine, and co-incubated with 10 μL RITC@PEI-L-/D-TA@MON solution (200 μg/mL, $n = 3$) for 30 min at 37 °C. 20 μL sample was aspirated on a dish and the Brownian motion trajectory was captured using CLSM at 37 fps. The video was recorded for 10 min and processed using Image J software. MSD and D_{eff} were calculated as

$$\mathrm{MSD}_\tau = (x_{(t+\tau)} - x_t)^2 + (y_{(t+\tau)} - y_t)^2 \quad (6)$$

$$D_{\mathrm{eff}} = \frac{\mathrm{MSD}}{4\tau} \quad (7)$$

where x and y represent the coordinates of the particles and τ indicates time intervals.

Intestinal mucosal adhesion assay

Colons were isolated from overnight fasted SD rats and DSS-model rats, gently rinsed with SIF, and cut into 1 cm × 4 cm segments placed on slides. RITC@PEI-L/D-TA@MON (10 mg, $n = 3$) were evenly sprinkled on the prepared intestinal tissues, fixed on a 45° operating platform, and incubated at 37°C for 15 min. Subsequently, SIF was used to elute the nanomedicines from the intestinal tissues for 5 min, and the eluent was collected to measure the fluorescence intensity (Ex/Em: 570/595 nm).

In addition, fluorescence images of the mucosa after elution was recorded using Living Image System (Night OWL II LB 983, Germany) and the RITC signal intensity was semi-quantified using indiGo software. Then, the mucosa was immediately fixed in formalin, embedded in OCT, freeze sliced, stained with DAPI, and observed by CLSM. Similarly, we performed mucosal adhesion experiments on ex vivo human intestinal mucosa, which was cut into 2 cm × 4 cm, following the same procedure.

Intestinal uptake and retention

Healthy mice and DSS-model mice were oral administrated with RITC@PEI-L/D-TA@MON (100 mg/kg, $n = 3$), respectively, and the colons were isolated after 2 h, fixed in formalin, embedded in OCT, freeze sliced, stained with DAPI, and observed by CLSM. Intestinal villus uptake was also performed on ex vivo human intestinal segments. Intestinal segments (5 cm) were ligated and incubated with 10 mL RITC@PEI-L/D-TA@MON (2 mg/mL, $n = 3$) suspend in Tyrode solution at 37°C. After 1.5 h, the intestinal segments were fixed, embedded, sectioned, stained with DAPI, and observed by CLSM.

To study the GIT retention of nanomedicines, healthy mice and DSS-model mice were fasted overnight and orally administered with RITC@PEI-L/D-TA@MON (100 mg/kg, $n = 3$) were. At preset time points, the whole GIT and the main organs were isolated for ex vivo imaging, and semi-quantitative determined the fluorescence intensity.

Biocompatibility

Firstly, the hemocompatibility of nanomedicines were evaluated by a hemolysis test. Venous blood was taken from SD rats after overnight fasting, centrifuged and washed to obtain red blood cells (RBCs), which were diluted with sterile saline to obtain 2% RBCs solution (v/v). 2 mL RBCs solution was mixed with equal volumes of normal saline suspension solution of PEI-L/D-TA@MON at different concentrations ($n = 3$). RBCs solution was mixed with equal volumes of normal saline and deionized water, and served as negative (-) and positive (+) control groups, respectively. After standing for 4 h, the supernatant was centrifuged and assayed by UV–Vis method ($\lambda_{max} = 540$ nm).

The in vivo toxicity of nanomedicines was investigated. Mice were orally administered with PEI-L/D-TA@MON (at double dose, 200 mg/

kg, $n = 3$) once daily for 7 days and weighed every two days. On day 14, whole blood and serum were collected from mice for hematological evaluation (BC-2800vet, Mindray, China) and biochemical analysis (poch-100i, Sysmex, Japan), respectively. In addition, key organs such as heart, liver, spleen, lungs, kidneys and GIT were isolated, weighed, and stained by HE. The intestines were also stained with ZO-1 and Occduin to examine the barrier integrity.

DSS-induced acute colitis model

To establish an acute ulcerative colitis model, C57BL/6 mice were fed with 3% (w/v) DSS solution instead of normal drinking water for 7 days. For prophylactic effect, DSS-model mice ($n = 6$) were given the normal saline suspension of nanomedicines (100 mg/kg) from day 2 to day 7 via oral administration. Mice in the control group were given normal saline for treatment, and mice in the normal group only received normal saline without DSS exposure. The body weight, water intake, and DAI score based on the body weight, blood in faeces, and faecal morphology of the animals were recorded daily. After two days of recovery, mice were euthanized at day 10. The serum and colon tissue were collected to investigate the cfDNA content, cytokine levels, and histopathological examinations. After length determination, colon tissue was fixed, embedded, stained with HE for histological studies, stained with antibodies against ZO-1, Occudin, CD86, CD206, CD31, F4/80, MPO, Ly6G, caspase3, CD4, CD8, GATA-3, Tbet and FoxP3 for IF studies, and stained with TLR1/2/4/5/9, MyD88, NK-κB, TNF-α and IL-1β for IHC studies. Colon tissues were mixed with pH 7.4 PBS at a ratio of 1:9 to prepare homogenates to detect the TNF-α, IL-1β, IL-4, IL-6, IL-10, IL-17, MCP-1 and IFN-γ levels according to the methods described in the ELISA kits (Elabscience, Wuhan). Colon tissues were also transferred to transcriptome analysis, wherein the total RNA was extracted, identified and quantified, followed by the reverse transcription of RNA to cDNA, amplification of primed cDNA by PCR and acquisition of RNA-seq. With respect to the transcriptome, the peritoneal macrophages from DSS mice in the control group and PEI-L-TA@MON treated group were isolated, suspended and incubated for 24 h. The adherent cells were lysed, separated the supernatant, and mixed with the Nonreducing SDS buffer. Samples were then separated on sodium dodecyl sulfate-polyacrylamide gel electrophoresis (SDS-PAGE) and transferred to polyvinylidene fluoride (PVDF) (ISEQ00010, Millipore) membranes. By using GAPDH as the internal control, blots were incubated with TLR4, TLR9, MyD88, NF-κB p65 (phospho S536), NF-κB p65 and GAPDH antibodies, and treated with HRP-conjugated secondary antibody, wherein the bands were analyzed by ECL detection system (GelView 6000Pro, BLT).

FCM was used to determine the ratio of Treg, Th1 and Th2 cells, and the spleens of mice in each group were removed and ground in petri dishes containing 1 mL RPMI1640 complete medium. The filtrate was filtered using a 70 um sterile filter (Absin, Shanghai) and then rinsed by adding cell culture medium and collecting the filtrate. The cell suspension was centrifuged at 4 °C, 500 g for 5 min. 2 mL of erythrocyte lysate (Solarbio, Beijing) was added to resuspend the cells after discarding the supernatant, and the cells were lysed on ice for 2 min before centrifugation. Discard the supernatant and resuspend the cells with 100 uL of PBS, add 5 uL of CD4 and CD25 antibodies (BD Pharmingen, America), incubate at 4 °C for 25 min, resuspend the cells with 1.8 mL of PBS (containing 1% BSA) and centrifuge the cells, discard the supernatant and add 200 uL of PBS, 200 uL of Fixation buffer (Elabscience, Wuhan) and incubate for 30 min, avoiding light. 1 mL of 1× Permeabilization Working Solution (Elabscience, Wuhan) was added and centrifuged. Centrifuge and discard the supernatant, add 100 uL Permeabilization Working Solution, resuspend, add 5 uL Foxp3, IL-4, IFN-γ antibody, incubate for 30 min, avoid light, add 1.8 mL PBS (containing 1% BSA). Add 1.8 mL PBS (containing 1% BSA). After centrifugation and discarding the supernatant, add 400 uL of PBS and resuspend, 300 mesh nylon mesh filter on the machine.

For therapeutic effect, diseased mice treated with DSS were orally administered daily with PEI-L-TA@MON (100 mg/kg, $n = 6$) from day 5 to day 11, and normal mice were given PBS. Body weight, water intake and DAI score of the animals were recorded every day. After two days of recovery, mice were sacrificed on day 14. Faeces were collected for 16S examination, serum was removed for cfDNA study, and colonic tissues were isolated for length determination, cytokine detection and histopathological examination.

Drug loading and release

Five clinical first-line or second line drugs, including non-steroidal anti-inflammatory drug Mes, immunosuppressant Tac, glucocorticoid Dex, plant sources antibacterial drug Ber and antibiotic Nor were chosen to in situ load into PEI-L-TA@MON. Along with the synthesis of PEI-L-TA@MON, 40 mg drug was per-dissolved in the water or ethanol according to their solubility to obtain Drug/PEI-L-TA@MON.

To study the physicochemical properties and crystalline state of Drug/PEI-L-TA@MON, we performed FTIR and XRD analyses before and after drug loading. We also recorded the FTIR and XRD spectra of Drug/PEI-L-TA@MON after prolonged storage at room temperature for 6 months to confirm their physical stability.

Subsequently, in vitro drug release experiments were carried out on a ZRS-8G dissolution tester (Tianjin XinTianGuang Analytical Instrument Technology Co., Ltd., China) by reference to the small cup method. In a typical run, drug or Drug/PEI-L-TA@MON (equivalent to 5 mg drug, n = 3) was exposed to 250 mL of SIF with a stirring rate of 100 rpm/min. 3 mL sample was taken at pre-specified time intervals, passed through a microporous filter membrane and sent to microplate reader in UV mode to determine the drug concentration by standard curve. Meanwhile, the same volume SIF was immediately replenished to keep a constant volume.

Drug/PEI-L-TA@MON intestinal retention and absorption

Drugs or Drug/PEI-L-TA@MON (dose equivalent to 1 mg drug, $n = 3$) were exposed onto intestinal segments (1 cm × 4 cm) isolated from SD rats, and eluted by SIF for 5 min. The eluent was collected every 1 min, centrifuged, and sent to microplate reader in UV mode to determine the drug concentrations by standard curves.

With the aim of studying the functionality of PEI-L-TA@MON as oral drug carrier, freshly isolated rat small intestines were cut into 10 cm segments, turned out the mucosal side, ligated both ends, and injected 2 mL Tyrode solution into the inside serosal side. Afterwards, the system was immersed in 15 mL drug or Drug/PEI-L-TA@MON Tyrode solution suspensions (equivalent to 5 mg drug, $n = 3$) at 37 °C. At 0.5, 1, 2, 3, and 4 h post incubation, 150 µL solution was taken out from the inside serosal side, followed by injection of 150 µL Tyrode solution. After centrifugation, drug contents were monitored based on the standard curves by microplate reader in UV mode.

Synergistic therapy of PEI-L/D-TA@MON

C57BL/6 mice were fed with 3% (w/v) DSS solution instead of normal drinking water for 7 days to establish an acute ulcerative colitis model. As per prophylactic treatment administration, DSS model mice ($n = 6$) were given drug (40 mg/kg) and Drug/PEI-L-TA@MON (equivalent to drug 40 mg/kg) orally from day 2 to day 7. Control mice were given saline treatment and normal mice were given only saline without exposure to DSS. For nanomedicine alone, we also set a PEI-L-TA@MON group treated with PEI-L-TA@MON (100 mg/kg, $n = 6$). The body weights and DAI scores of the animals were recorded daily. After two days of recovery, the mice were euthanized on day 10. After length determination, colon tissues were used to detect cytokine levels. A homogenate was prepared by mixing colon tissue with pH 7.4 PBS at a ratio of 1:9, and TNF-α, IL-1β, IL-4, IL-6, IL-10, IL-17, MCP-1, and IFN-γ levels were detected according to the method described in the ELISA

kit (Elabscience, Wuhan). Other colon tissues were fixed, embedded, and stained with HE for histological studies.

Statistical analysis

All experiments were performed in three parallel groups, except for the animal experiments, which were performed in six parallel groups. All data were expressed as mean and standard deviation (SD). Two tailed Student's *t* test and One-way ANOVA was applied to compare experimental groups. A *P*-value < 0.05 was considered statistically significant. The levels of significance were set at the probability of $^{*}P < 0.05$, $^{**}P < 0.01$, and $^{***}P < 0.001$.

Reporting summary

Further information on research design is available in the Nature Portfolio Reporting Summary linked to this article.

Data availability

The source data generated in this study are provided in the Supplementary Information/Source Data file. The source data generated in this study have been deposited in the Figshare database under DOI code https://doi.org/10.6084/m9.figshare.28386470 [https://doi.org/10.6084/m9.figshare.28386470]. The sequencing data used in this study are available in the NCBI Sequence Read Archive (SRA) database under BioProject accession code PRJNA1222285. All the other data that support the findings of this study are available within the Article and its Supplementary Information files and from the corresponding author. Source data are provided with this paper.

References

1. Le, B. C., Honap, S. & Peyrin-Biroulet, L. Ulcerative colitis. *Lancet* **12**, 571–584 (2023).
2. Little, R. D. et al. Pathogenesis and precision medicine for predicting response in inflammatory bowel disease: advances and future directions. *eGastroenterology* **2**, 1 (2024).
3. Kaplan, G. G. & Ng, S. C. Understanding and preventing the global increase of inflammatory bowel disease. *Gastroenterology* **152**, 313–321 (2017).
4. Noble, A. J., Nowak, J. K., Adams, A. T., Uhlig, H. H. & Satsangi, J. Defining interactions between the genome, epigenome, and the environment in inflammatory bowel disease: progress and prospects. *Gastroenterology* **165**, 44–60 (2023).
5. Bao, W. et al. Aloe emodin promotes mucosal healing by modifying the differentiation fate of enteroendocrine cells via regulating cellular free fatty acid sensitivity. *Acta Pharm. Sin. B* **14**, 3964–3982 (2024).
6. Liu, J., Di, B. & Xu, L. L. Recent advances in the treatment of IBD: Targets, mechanisms and related therapies. *Cytokine Growth Factor Rev.* **71-72**, 1–12 (2023).
7. Ramos, G. P. & Papadakis, K. A. Mechanisms of disease: inflammatory bowel diseases. *Mayo Clin. Proc.* **94**, 155–165 (2019).
8. Luo, H. et al. Emerging pharmacotherapy for inflammatory bowel diseases. *Pharm. Res.* **178**, 106146 (2022).
9. Zhang, X. et al. ROS-triggered self-disintegrating and pH-responsive astaxanthin nanoparticles for regulating the intestinal barrier andcolitis. *Biomaterials* **292**, 121937 (2023).
10. Pan, X., Zhu, Q., Pan, L. L. & Sun, J. Macrophage immunometabolism in inflammatory boweldiseases: From pathogenesis to therapy. *Pharm. Ther.* **238**, 108176 (2022).
11. Shi, C. et al. A nanoparti-culate dual scavenger for targeted therapy of inflammatory bowel disease. *Sci. Adv.* **28**, eabj2372 (2022). 8.
12. Solitano, V. et al. Efficacy and safety of a-dvanced oral small molecules for inflammatory bowel disease: systematic review and meta-analysis. *J. Crohns Colitis* **24**, 1800–1816 (2023). 17.
13. Rubin, D. T., Ananthakrishnan, A. N., Siegel, C. A., Sauer, B. G. & Long, M. D. ACG clinical guideline: ulcerative colitis in adults. *Am. J. Gastroenterol.* **114**, 384–413 (2019).
14. Targan, S. R. Current limitations of IBD treatment: where do we go from here? *Ann. NY Acad. Sci.* **1072**, 1–8 (2006).
15. Yin, L. et al. Phytoconstituent-derived nano-medicines/vesicles providing a promising dawn for inflammatory bowel disease. *Chin. Chem. Lett.* 110224 (2024).
16. Tabas, I. & Glass, C. K. Anti-inflammatory therapy in chronic disease: challenges and opportunities. *Science* **339**, 166–172 (2013).
17. Lobaton, T., Vermeire, S., Van Assche, G. & Rutgeerts, P. anti-adhesion therapies for inflammatory bowel disease. *Aliment Pharm. Ther.* **39**, 579–594 (2014).
18. Weng, H. et al. The complexation of insulin with sodium N-[8-(2-hydroxybenzoyl) amino]-caprylate for enhanced oral delivery: Effects of concentration, ratio, and pH. *Chin. Chem. Lett.* **33**, 1889–1894 (2022).
19. Wang, Y. et al. Chiral mesoporous silica nano-screws as an efficient biomimetic oral drug delivery platform through multiple topological mechanisms. *Acta Pharm. Sin. B.* **12**, 1432–1446 (2022).
20. Laroui, H. et al. Fab'-bearing siRNA TNFalpha-loaded nanoparticles targeted to colonic macrophages offer an effective therapy for experimental colitis. *J. Control Rel.* **186**, 41–53 (2014).
21. Zu, M. et al. Oral delivery of natural active small molecules by polymeric nanoparticles for the treatment of inflammatory bowel diseases. *Adv. Drug Deliv. Rev.* **176**, 113887 (2021).
22. Wei, X. et al. Caffeic acid phenethyl ester loaded in a targeted delivery system based on a solid-in-oil-in-water multilayer emulsion: characterization, stability, and fate of the emulsion during in vivo digestion. *Food Res. Int.* **161**, 111756 (2022).
23. Wang, J. et al. Mitochondria-targeting folic acid-modified nano-platform based on mesoporous carbon and a bioactive peptide for improved colorectal cancer treatment. *Acta Biomater.* **15**, 453–472 (2022).
24. Yang, J. et al. From the updated landscape of the emerging biologics for IBDs treatment to the new delivery systems. *J. Control Rel.* **361**, 568–591 (2023).
25. Ocansey, D. K. et al. Exosome-mediated effects and applications in inflammatory bowel disease. *Biol. Rev. Camb. Philos. Soc.* **95**, 1287–1307 (2020).
26. Duan, Y., Zhang, E., Fang, R. H., Gao, W. & Zhang, L. Capsulated cellular nanosponges for the treatment of experimental inflammatory bowel disease. *ACS nano* **17**, 15893–15904 (2023).
27. Pu, Y. et al. Harnessing polymer-derived drug delivery systems for combating inflammatory bowel disease. *J. Control Rel.* **354**, 1–18 (2023).
28. Han, Y. et al. Biomimetic aminoated mesoporous silica xerogel exhibiting chiral surface topology for delivery insoluble drug with multiple-controlled manners and improved oral adsorption. *Mater. Des.* **223**, 111157 (2022).
29. Chen, X. et al. Chiral nanosilica drug delivery systems stereoselectively interacted with the intestinal mucosa to improve the oral adsorption of insoluble drugs. *ACS Nano* **17**, 3705–3722 (2023).
30. Jin, R. H. & Yuan, J. J. (2005). Simple synthesis of hierarchically structured silicas by poly (ethyleneimine) aggregates pre-organized by media modulation. *Macromol. Chem. Phys.* **206**, 2160–2170 (2005).
31. Matsukizono, H. & Jin, R. H. High-temperature-resistant chiral silica generated on chiral crystalline templates at neutral pH and ambient conditions. *Angew. Chem.* **24**, 5964–5967 (2012).
32. Naik, R. R. et al. Controlled formation of biosilica structures in vitro. *Chem. Commun.* 238–239 (2003).
33. Nie, D. et al. Cancer-cell-membrane-coated nanoparticles with a yolk-shell structure augment cancer chemotherapy. *Nano Lett.* **20**, 936–946 (2020).
34. Wu, X. et al. A microenvironment-responsive graphdiyne-iron nanozyme hydrogel with antibacterial and anti-inflammatory effect for periodontitis treatment. *Adv. Healthc. Mater.* e2403683 (2024).

35. Liu, Y. et al. Integrated cascade nanozyme catalyzes in vivo ROS scavenging for anti-inflammatory therapy. *Sci. Adv.* **6**, eabb2695 (2020).
36. Yang, Y. et al. Prodrug nanoassemblies bridged by Mono-/Di-/Tri-sulfide bonds: exploration is for going further. *Nano Today* **44**, 101480 (2022).
37. Shao, D. et al. Bioinspired diselenide-bridged mesoporous silica nanoparticles for dual-responsive protein delivery. *Adv. Mater.* **30**, 1801198 (2018).
38. Wang, X. et al. Plasmonic supramolecular nanozyme-based bio-cockleburs for synergistic therapy of infected diabetic wounds. *Adv. Mater.* **36**, e2411194 (2024).
39. Zhao, S. et al. An orally administered CeO_2 @montmorillonite nanozyme targets inflammation for inflammatory bowel disease therapydv. *Funct. Mater.* **30**, 2004692 (2020).
40. Wang, J. et al. Microenvironment responsive pod-structured astaxanthin nanocarrier for ameliorating inflammatory bowel disease. *Chin. Chem. Lett.* **35**, 109029 (2024).
41. Zhou, Y. et al. Mesoporous silica nanoparticles for drug and gene delivery. *Acta Pharmaceutica Sin. B* **8**, 165–177 (2018).
42. Richards, D. M. & Endres, R. G. The mechanism of phagocytosis: two stages of engulfment. *Biophys. J.* **107**, 1542–1553 (2014).
43. Behzadi, S. et al. Cellular uptake of nanoparticles: journey inside the cell. *Chem. Soc. Rev.* **46**, 4218–4244 (2017).
44. Wang, Y. et al. Enantioselective oral absorption of molecular chiral mesoporous silica nanoparticles. *Adv. Mater.* **35**, 2307900 (2023).
45. Mousazadeh, H., Bonabi, E. & Zarghami, N. Stimulus-responsive drug/gene delivery system based on polyethylenimine cyclodextrin nanoparticles for potential cancer therapy. *Carbohydr. Polym.* **276**, 118747 (2022).
46. Ren, J. et al. Self-assembled polymeric micelle as a novel mRNA delivery carrier. *J. Controlled Rel.* **338**, 537–547 (2021).
47. Zhang, X. et al. An orally-administered nanotherapeutics with carbon monoxide supplying for inflammatory bowel disease therapy by scavenging oxidative stress and restoring gut immune homeostasis. *ACS Nano* **17**, 21116–21133 (2023).
48. Min, D. K. et al. Orally administrated inflamed colon-targeted nanotherapeutics for inflammatory bowel disease treatment by oxidative stress level modulation in colitis. *ACS Nano* **17**, 24404–24416 (2023).
49. Wang, Y. et al. Abelmoschus manihot polysaccharide fortifies intestinal mucus barrier to alleviate intestinal inflammation by modulating Akkermansia muciniphila abundance. *Acta Pharm. Sin. B* **14**, 3901–3915 (2024).
50. Niu, M. et al. Colon-specific controlled release of oral liposomes for enhanced chemo-immunotherapy against colorectal cancer. *Acta Pharm. Sin. B* **14**, 4977–4993 (2024).
51. Li, L. et al. Diagnosis and management of inflammatory bowel disease. *J. Evid. Based Med.* **17**, 409–433 (2024).

Acknowledgements

This work was supported by the National Natural Science Foundation of China (No. 82472136 [H.L.], No.82373229[L.Z.]).

Author contributions

H.L. and L.Z. conceived the concept and directed the project. M.X. performed the main experimental work. W.X. collected and analyzed the patient specimens. J.X., A.W., and S.M. helped with all cellular experiments. D.D., Y.W., and D.Y. assisted with the animal sections. H.L., M.X., and W.X. wrote the manuscript. All authors discussed and commented on the manuscript.

Competing interests

The authors declare no competing interests.

Additional information

Supplementary information The online version contains supplementary material available at https://doi.org/10.1038/s41467-025-57890-8.

Correspondence and requests for materials should be addressed to Lin Zhao or Heran Li.

Peer review information *Nature Communications* thanks Lei Chen, Ying-Wei Yang, and the other, anonymous, reviewer(s) for their contribution to the peer review of this work. A peer review file is available.